J. Fluid Mech. (2003), *vol.* 485, *pp.* 243–277.
DOI: 10.1017/S002211200300452X Printed in the United Kingdom

Experimental study of the Richtmyer–Meshkov instability of incompressible fluids

By C. E. NIEDERHAUS† AND J. W. JACOBS

Department of Aerospace and Mechanical Engineering, University of Arizona, Tucson, AZ 85721, USA

(Received 23 July 2002 and in revised form 24 January 2003)

The Richtmyer–Meshkov instability of a low-Atwood-number miscible two-liquid system is investigated experimentally. The initially stratified fluids are contained within a rectangular tank mounted on a sled that rides on a vertical set of rails. The instability is generated by dropping the sled onto a coil spring, producing a nearly impulsive upward acceleration. The subsequent free-fall that occurs as the container travels upward and then downward on the rails allows the instability to evolve in the absence of gravity. The interface separating the two liquids initially has a well-defined sinusoidal perturbation that quickly inverts and then grows in amplitude after undergoing the impulsive acceleration. Disturbance amplitudes are measured and compared to theoretical predictions. Linear stability theory gives excellent agreement with the measured initial growth rate, $\dot{a}_0$, for single-mode perturbations with the predicted amplitudes differing by less than 10% from experimental measurements up to a non-dimensional time $k\dot{a}_0 t = 0.7$, where k is the wavenumber. Linear stability theory also provides excellent agreement for the individual mode amplitudes of multi-mode initial perturbations until the interface becomes multi-valued. Comparison with previously published weakly nonlinear single-mode models shows good agreement up to $k\dot{a}_0 t = 3$, whereas published nonlinear single-mode models provide good agreement up to $k\dot{a}_0 t = 30$. The effects of Reynolds number on the vortex core evolution and overall growth rate of the interface are also investigated. Measurements of the overall amplitude are found to be unaffected by the Reynolds number for the range of values studied here. However, experiments carried out at lower values of Reynolds numbers were found to have decreased vortex core rotation rates. In addition, an instability in the vortex cores is observed. The time of appearance of this instability was found to increase when the Reynolds number is decreased.

1. Introduction

Richtmyer–Meshkov (RM, Richtmyer 1960; Meshkov 1969) instability is the instability of an impulsively accelerated planar interface separating two fluids of different density. For example, RM instability causes small perturbations on a flat interface, accelerated by a passing shock wave, to grow in amplitude and eventually become a turbulent flow. RM instability is closely related to Rayleigh–Taylor (RT, Rayleigh 1900; Taylor 1950) instability, which is the instability of a planar interface undergoing constant acceleration, such as caused by the suspension of a heavy fluid over a lighter one in the Earth's gravitational field. Therefore, RM instability is often referred

† Present address: NASA Glenn Research Center, 21000 Brookpark Road, Cleveland, OH 44135, USA.

to as impulsive or shock-induced Rayleigh–Taylor instability. The simplicity of RM instability (in that it requires very few defining parameters), and the ability to generate it in a closed container, makes it an excellent fluid flow for the study of nonlinear stability theory as well as turbulent transport in a heterogeneous system. The fact that RM instability is a fundamental hydrodynamic instability that exhibits all of the nonlinear complexities that transform simple initial conditions into a complex turbulent flow make it a popular benchmark for computational fluid dynamics codes.

RM instability is of importance to a variety of applications spanning a wide range of scales. For example, at very large scales, RM instability results in mixing in supernovas. During a supernova explosion, an outward propagating spherical shock wave formed in the collapsing core of a dying star passes through stratified outer gas layers of differing density producing RM instability. Observations of Supernova 1987A indicate that the helium and hydrogen outer layers experienced a significant amount of RM induced mixing as a result of this event (Arnett *et al.* 1989; Burrows, Hayes & Fryxell 1995). RM instability can also occur in high-speed combustion applications such as in supersonic combustion ramjet engines (scramjets) in which mixing the fuel and air is a significant challenge. One proposed solution to this problem is to pass a light gaseous hydrogen fuel jet surrounded by the (heavy) air free stream through an oblique shock wave. The resulting RM instability increases the mixing, yielding an augmentation of the burning rate (Markstein 1957; Curran, Heiser & Pratt 1996). At even smaller scales, RM instability is of fundamental importance in inertial confinement fusion (ICF). ICF uses high-energy laser beams to compress a shell encapsulating a low-density deuterium–tritium fuel mixture. The shell–fuel density interface undergoes a combination of RM and RT instabilities resulting in a turbulent flow that limits the degree of compression achievable in this process. These instabilities are the most significant reason why, in the experiments conducted to date, the energy used to drive the lasers has greatly exceeded the energy output from the fusion process (McCall 1983; Lindl, McCrory & Cambell 1992; Hogan, Bangerter & Kulcinski 1992; Lindl 1995).

Taylor (1950) was the first to use linear stability theory to analyse the growth of perturbations on a flat interface in a constant gravitational field. Using potential flow to describe the velocity field in each of the fluids, Taylor showed that the amplitude of a small two-dimensional sinusoidal perturbation $\eta(x, t) = a(t)\cos(kx)$ given to a system with a heavy fluid with density ρ_2 over a lighter one with density ρ_1 evolves according to:

$$a = a_0 \cosh\left(\sqrt{kgA}\, t\right), \tag{1}$$

where $A = (\rho_2 - \rho_1)/(\rho_2 + \rho_1)$ is the Atwood number and a_0 is the initial amplitude. Thus, a system oriented with a heavy fluid over a lighter one will grow exponentially in time, and the oppositely oriented configuration (light fluid over heavy) generates oscillating solutions, indicating stability. Richtmyer (1960) addressed the instability of a planar interface separating two gases that is impulsively accelerated by a planar shock wave travelling in the direction of the normal to the interface. He recognized that for relatively weak shocks, this problem could be modelled adequately by considering incompressible fluids in an impulsive gravitational field. Thus, he modelled the instability using the same techniques as Taylor, except for using a gravitational force in the form of a Dirac delta function ($g(t) = \Delta V \delta(t)$) and obtained the following expression for the growth rate of the perturbation:

$$\dot{a} = kA\Delta V\, a_0, \tag{2}$$

where ΔV is the velocity change imparted by the impulsive acceleration and a_0 is the initial amplitude. Thus, small perturbations to the flat interface result in a constant growth rate, but, unlike the constant acceleration case, the instability occurs whether the acceleration is directed from light fluid to heavy or vice versa. When the acceleration is directed from the lighter into the heavier fluid, the resulting body force has a similar orientation to that producing Rayleigh–Taylor instability. Thus, the amplitude monotonically increases at a constant rate. Conversely, when the acceleration is oppositely directed, the amplitude first decreases until it passes through zero, after which it emerges as a growing waveform that has been shifted in phase by 180°.

The linear growth stage described by Richtmyer's result lasts as long as the perturbation amplitude is sufficiently small (typically, as long as $ka < 1$). When the amplitude becomes comparable to the wavelength, the growth rate of the exact solution decreases owing to the influence of the nonlinearity of the governing equations. The effects of weak nonlinearity can be incorporated into the stability analysis by developing a solution in the form of an asymptotic expansion using the perturbation amplitude as the small parameter (Haan 1991). These solutions, however, have the weakness that when truncated they produce results that quickly diverge from the exact solution when the amplitude reaches moderate size. Zhang & Sohn (1997) have found a solution to this problem by posing their series solution as a Padé approximant which significantly extends its validity. One shortcoming of Zhang & Sohn's solution is that it does not possess the generally accepted asymptotic behaviour that the growth rate decays as $1/t$ as time, t, approaches infinity. This weakness has been addressed by Sadot *et al.* (1998) who present a model that both captures the initial weakly nonlinear behaviour and also provides the correct late-time asymptotic form.

The impulsive acceleration in RM instability is typically produced by the passage of a shock wave over the interface. The most common method for generating RM instability in the laboratory is to create a boundary between two gases in a shock tube. Early shock tube RM experiments used a physical barrier to separate the two gases initially in order to prevent their mixing. However, physical barriers subsequently introduce other difficulties. The earliest of these methods, used by Meshkov (1969) and others (Aleshin *et al.* 1988; Benjamin 1992; Vassilenko *et al.* 1992), employs a sinusoidally shaped thin membrane between the two gases to separate them and provide the initial perturbation. This membrane is subsequently shattered by the incident shock wave. However, the pieces of the membrane become incorporated into the fluid flow, impeding visualization and potentially affecting the development of the instability. Furthermore, this method often produces initial growth rate measurements that are significantly less than Richtmyer's theoretical prediction, typically by a factor of two or more.

Another method for interface formation employs a thin plate to separate the gases (Cavailler *et al.* 1990; Brouillette & Sturtevant 1994; Bonazza & Sturtevant 1996). When extracted prior to shock tube firing, the wake produced by the plate provides a pseudosinusoidal perturbation to the interface. The results of these experiments are limited by the fact that the initial perturbation is uncontrolled, non-uniform and often unrepeatable. As is characteristic of all fluid instabilities, the initial state of the system dictates future behaviour, hence any variation in initial conditions makes it difficult to compare experimental results from experiment to experiment. The interfaces created by this method are also very diffuse, having thicknesses equalling or exceeding the perturbation wavelength, which significantly slows instability growth. More recently,

experiments studying the RM instability of two nearby interfaces using a gas curtain (Jacobs *et al.* 1993, 1995; Budzinski, Benjamin & Jacobs 1994; Rightley *et al.* 1999) have successfully produced membraneless experiments which use advanced diagnostic techniques. However, gravitational effects make this technique ineffective for the generation of single-interface configurations in a horizontal shock tube.

An alternative method for forming the interface between two gases was developed by Jones & Jacobs (1997). In these experiments, the two gases flowed from opposite ends of the vertical shock tube, exiting through slots at the initial interface location. The result was a relatively thin interface between the fluids that was sinusoidally perturbed by laterally oscillating the entire shock tube to form a standing wave. This method eliminates the influence of a membrane, yet it also provides repeatable initial conditions. These experiments have yielded initial growth rate measurements that are in much better agreement with linear and weakly nonlinear analyses than previous experiments.

In response to difficulties associated with the generation of interfaces between gases in shock tube experiments, a number of researchers have developed alternative experimental methods employing shock accelerated liquids or solids to produce the instability. The use of solids is particularly advantageous because of the relative ease with which a perturbation of known shape can be machined onto a solid surface. However, very strong shocks are necessary in order to make the solids behave as fluids. Benjamin & Fritz (1987) employed a shock wave generated by an explosive charge to liquefy a layer of Wood's metal in contact with a layer of water. The sinusoidal interface machined into the Wood's metal became RM unstable, causing the perturbations to invert and then grow in amplitude. However, the interface in these experiments is also stabilized by the presence of gravity, which reduces the growth rate and makes analysis difficult. A number of investigators (Dimonte & Remington 1993; Remington *et al.* 1994; Dimonte, Frerking & Schneider 1995; Peyser *et al.* 1995; Dimonte & Schneider 1997; Farley *et al.* 1999; Holmes *et al.* 1999) have conducted experiments in which very strong shock waves are driven through targets consisting of two solids in the Nova laser facility at the Lawrence Livermore National Laboratory. In these experiments, the rapid vaporization of one end of a target produces a shock wave that travels through the density interface which has a machined initial perturbation. These experiments have demonstrated good agreement with linear and weakly nonlinear theory. However, problems associated with X-ray visualization and the difficulty in producing a pure impulsive acceleration in a laser facility make these experiments difficult to interpret.

Richtmyer (1960) recognized that RM instability need not be considered solely as a compressible phenomena in that the instability can be produced by impulsively accelerating incompressible fluids. Thus, a number of experimental studies have used this to study the incompressible RM instability. These experiments have the advantage that it is relatively easy to produce a sharp well-defined interface between two liquids. In addition, these experiments can be carried out at considerably lower speed than shock generated experiments, thus greatly simplifying flow visualization. Dimonte & Schneider (2000) developed a linear electric motor (LEM) apparatus to accelerate a container filled with two different density liquids vertically on a rail system. The LEM is capable of producing a variety of acceleration profiles, including constant and impulsive acceleration profiles which have been used to study RT and RM instabilities, respectively. The interface between the fluids was initially nominally flat, thus the primary focus of these experiments was to study the growth of the fully turbulent instability. Jacobs & Sheeley (1996) carried out significantly lower-speed

RM instability experiments in which they developed a novel technique for impulsively accelerating a system of two liquids. In these experiments, a Plexiglas tank containing two unequal density liquids is mounted to a linear rail system constraining its main motion to the vertical direction. The tank is gently oscillated horizontally to produce a controlled initial fluid interface shape. The sled is then released from an initial height and allowed to fall until it bounces off a fixed spring, which imparts an impulsive acceleration in the upward direction. After bouncing, the tank travels upward and then downward on the rail system while the instability develops. Note that the effects of gravity become increasingly important as the instability growth rate is decreased. The effects of gravity are minimized in these experiments by keeping the fluids in free-fall while the instability is allowed to develop.

The experiments reported here use the method developed by Jacobs & Sheeley, improved by the implementation of planar laser induced fluorescence (PLIF) imaging, yielding much clearer views of the developing interface. In addition, the experimental apparatus has been significantly improved by increasing the time duration in free-fall, direct measurement of the acceleration profile, and by allowing the generation of more complex initial perturbations.

2. Experimental methods

The experiments were conducted using a 3 m drop tower and sled with attached instrumentation, as shown in figure 1. The drop tower's function is to provide an impulsive acceleration to the two-fluid system, and then allow the system to travel safely in free-fall without external disturbances. The tower was developed using experience gathered from the earlier apparatus of Jacobs & Sheeley (1996). Note that the apparatus used in this study has also been used in a modified form for Rayleigh–Taylor experiments (Wadell, Niederhaus & Jacobs 2001). The tower consists of two pieces of vertical, 3 m long, square steel tubing with precision linear rails mounted on the inside faces. The sled travels on the linear rails at speeds up to $6\,\mathrm{m\,s^{-1}}$ using low-friction high-speed bearings. A retractable spring is mounted on vertical channels behind the drop tower. The sled is able to contact the extended spring, but passes freely when the spring is fully retracted. A shock absorber at the bottom of the rails stops the sled at the end of the experiment. The sled centre of mass is oriented to be centred between the linear rails and directly above the spring contact point to minimize vibrations during operation.

The two fluids are contained in a clear Plexiglas tank mounted to the sled using horizontal crossed roller bearings. The tank has interior dimensions of 254.4 mm in height and 119.9 mm in width (the horizontal dimension in the plane of the rails). Tanks having two different thicknesses (the horizontal dimension parallel to the observer's line of sight) were used. A 25.4 mm thick tank was used for the initial experiments. However, a thicker 50.8 mm tank was used for the majority of the experiments to minimize wall effects in the centre portion of the tank. An initial sinusoidal perturbation is imposed on the density interface by gently oscillating the tank horizontally at the proper frequency to produce $n + \frac{1}{2}$ standing internal waves, where n was varied from 0 to 4. The viscous boundary layers on the sidewalls of the tank require the slight modification of the frequency predicted by inviscid theory. Thus, a separate experimental investigation was undertaken to determine the precise forcing frequency necessary to ensure clean single-mode perturbations. The resulting perturbations have a measured wavelength prior to spring impact that is typically 3% greater than that predicted by inviscid theory based on tank width.

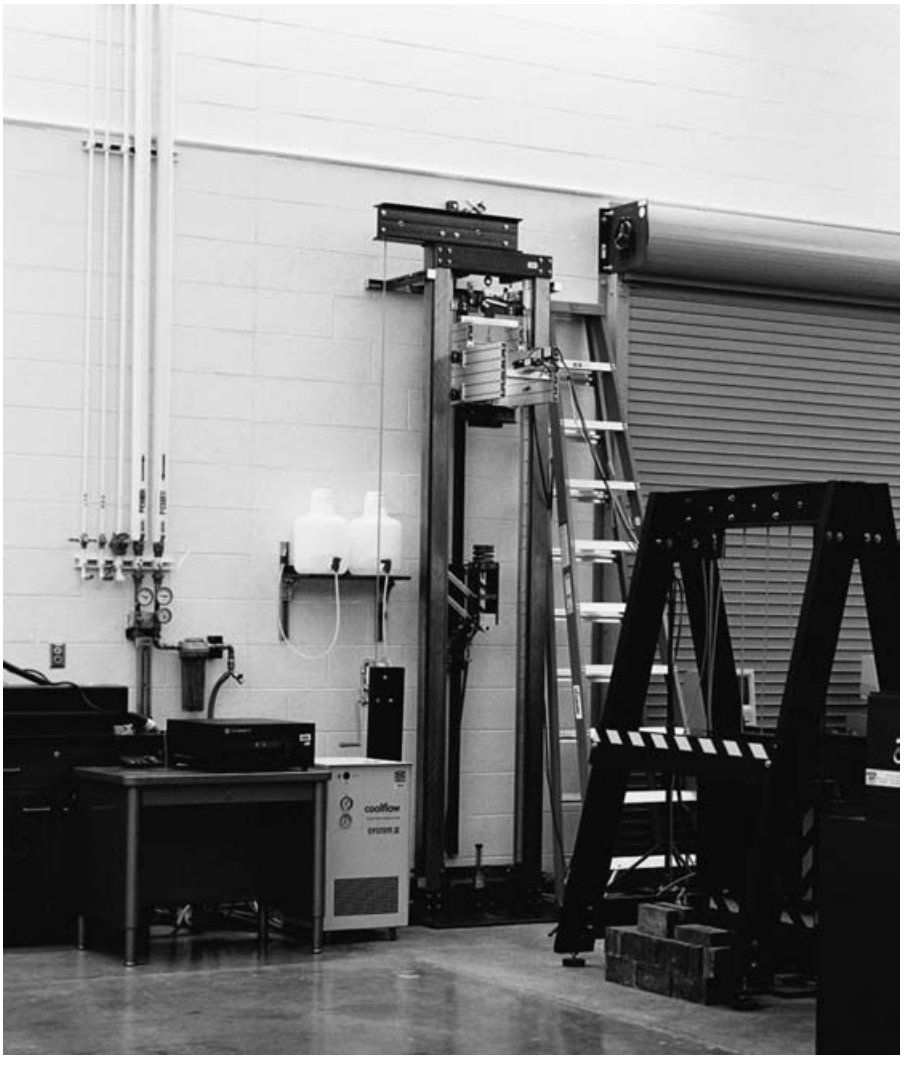

FIGURE 1. The 3 m drop tower with the sled positioned at the top of the rails.

The tank oscillation system has the capability to generate arbitrary motion. This capability allows a sinusoidal motion with the appropriate frequency and amplitude to produce a single-mode perturbation of the desired wavelength and amplitude. It also allows motion composed of a combination of different sine waves to produce more complex initial perturbations. Multi-mode initial perturbations are generated by oscillating the container with the superposition of the oscillations required for two or more individual modes. In both the single- and multi-mode experiments, the oscillation is stopped prior to sled release at the point where the tank oscillation velocity of all modes is zero. Single mode experiments presented here are limited to modes with $2\frac{1}{2}$ waves or fewer to reduce three-dimensional effects that occur in higher modes in the thicker (50.8 mm) tank.

Planar laser-induced fluorescence is used for flow visualization. A laser sheet generated from an argon-ion laser with an output of 2.8 W at 488 nm illuminates the centreplane of the fluid tank. The laser sheet intensity has a Gaussian distribution

and a width such that the intensity is 10% lower at the tank edges than at the centre. The sheet is 4 mm thick at its 50% power points at the tank location. Disodium fluorescein dye is added to the heavier lower fluid at a concentration of $0.84\,\mathrm{mg\,l^{-1}}$ which fluoresces when illuminated by the laser sheet. The lighter upper fluid is clear against a black background, allowing for easy distinction of the density interface. A double-speed CCD camera mounted on the sled captures images of the fluids at a resolution of 648×484 pixels at 60 Hz. The images are digitized and stored in real-time by a computer video acquisition system for later analysis. The relatively uniform laser illumination coupled with the low dye concentration yields images in which the fluorescent intensity is approximately proportional to the dye concentration. No effort was made to correct the images for light sheet non-uniformity or dye absorption to obtain the actual dye concentration levels.

The lighter fluid used in these experiments was a water/isopropanol mixture with a 70% volume concentration of isopropanol. The heavier fluid was a water/calcium nitrate salt solution with a 25% by weight calcium nitrate concentration. These two fluids are miscible and therefore have no surface tension. Batches of fluids were mixed with sufficient volume to conduct 5 to 10 experiments with one batch. The water/calcium nitrate solution was mixed to match the index of refraction of the current batch of the water/isopropanol mixture (purchased premixed). The matching of the index of refraction was necessary to eliminate distortion of the laser sheet as it passes through the highly curved interface present at late experimental times. The index of refraction and specific gravity of the mixtures varied slightly from batch to batch, but a typical batch had an index of refraction of 1.3720 and a specific gravity of 0.8731 for the lighter fluid and 1.2025 for the heavier fluid. The resulting Atwood number was 0.1587. The kinematic viscosity of the two liquids was measured for one batch using a viscometer. The lighter fluid was found to have a viscosity of 3.16 cSt, while the heavier fluid was 1.55 cSt.

To begin an experiment, the heavier bottom fluid was dispensed into the tank first to the desired level. A water-saturated piece of balsa wood slightly smaller than the interior dimensions of the tank was then placed on top of the heavy fluid. The lighter fluid was then dispensed at a slow rate immediately above the balsa wood through a small tube attached to a funnel. The balsa wood continued to float above the lighter fluid during the filling process. The tank was filled until the fluid level reached the top of the tank before the balsa wood was carefully removed. The centre portion of the tank lid protrudes 3.2 mm into the tank's interior. Installing the lid with a rolling motion forces out all air along with a small amount of fluid, resulting in a bubble-free environment inside the sealed tank. The total time required to add the lighter fluid, attach the lid, and begin the experiment was typically between 5 and 10 min. The resulting interface thickness was typically 1 pixel (0.21 mm) or less.

Figure 2 shows a sequence of three-dimensional renderings of the apparatus depicting an animation of a typical experiment. The sled is initially held at the top of the rails and the retractable spring mechanism is extended and locked. The tank is oscillated to produce the initial perturbation, and the sled released at the appropriate time. When the sled is released, it travels down the rails until it impacts the retractable spring and bounces upwards. As the sled travels back up the rails, the upward momentum from the recoil of the spring, together with the assistance of a bungee cord, unlocks the linkage holding the retractable spring mechanism. Gravity and the bungee assist retract the spring flush with the wall before the sled returns to the original spring location. The sled is then able to pass by the spring and travel down the rails until it impacts the shock absorber at the bottom of the rails. Thus, after the

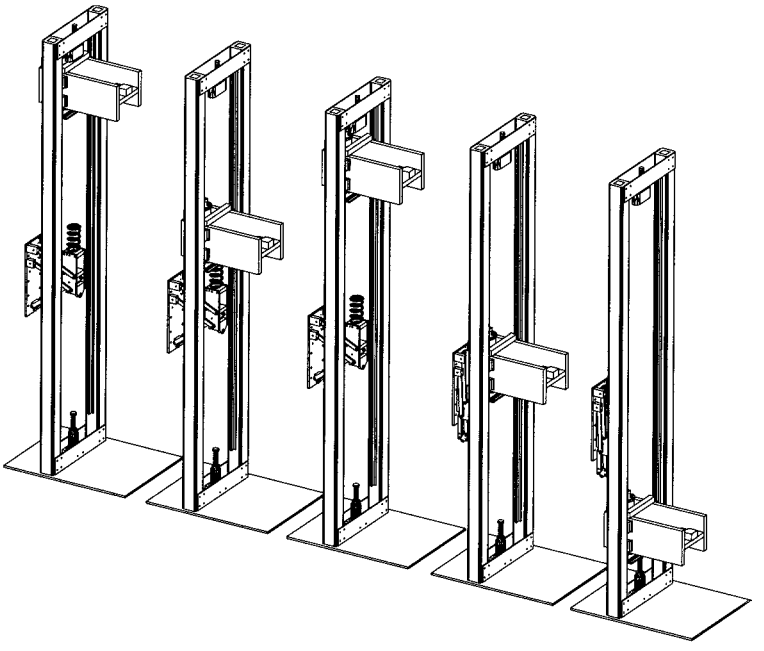

FIGURE 2. A sequence of images showing the sled travelling on the rail system during a typical experiment.

initial release, the fluids experience a nearly impulsive body force in the downward direction, followed by 900 ms of microgravity. A piezoelectric accelerometer was used to measure the impulsive acceleration, which typically peaked at approximately 50 g ($490\,\mathrm{m\,s^{-2}}$). A capacitive accelerometer was also used to measure the slight bearing drag during free-fall, which was typically less than 0.02 g ($0.2\,\mathrm{m\,s^{-2}}$).

3. Results and discussion

The simplest example of Richtmyer–Meshkov instability is that resulting from a small-amplitude single-mode sinusoidal initial perturbation on a sharp interface. Figure 3 is a sequence of PLIF images showing the evolution of such an instability. This particular experiment developed from a sinusodial perturbation with a dimensionless initial amplitude of $ka_i = 0.23$ and a wavelength λ corresponding to $1\frac{1}{2}$ waves inside the tank ($\lambda = 82.6\,\mathrm{mm}$), where $k = 2\pi/\lambda$ is the perturbation wavenumber and a_i is the perturbation initial amplitude. The visual streaks evident in the images taken at later times are the result of a slight mismatch in the index of refraction in the mixed region at the fluid interface. Although the refractive index for the two fluids was closely matched, diffusion at the fluid interface yields a thin region with a different refractive index. The observed streaks are the result of light rays passing through vertical sections of the interface where the mismatched index produces the largest deflection of the vertical light rays, creating an additional non-uniformity of the light sheet intensity. These effects are difficult to remove using standard algorithms for the correction of the effects of light absorption and laser sheet non-uniformity, thus no attempt was made to correct for this light intensity variation.

The first image in figure 3 was taken immediately before the sled impacted the spring and thus shows the initial interface shape. The impulsive acceleration in these

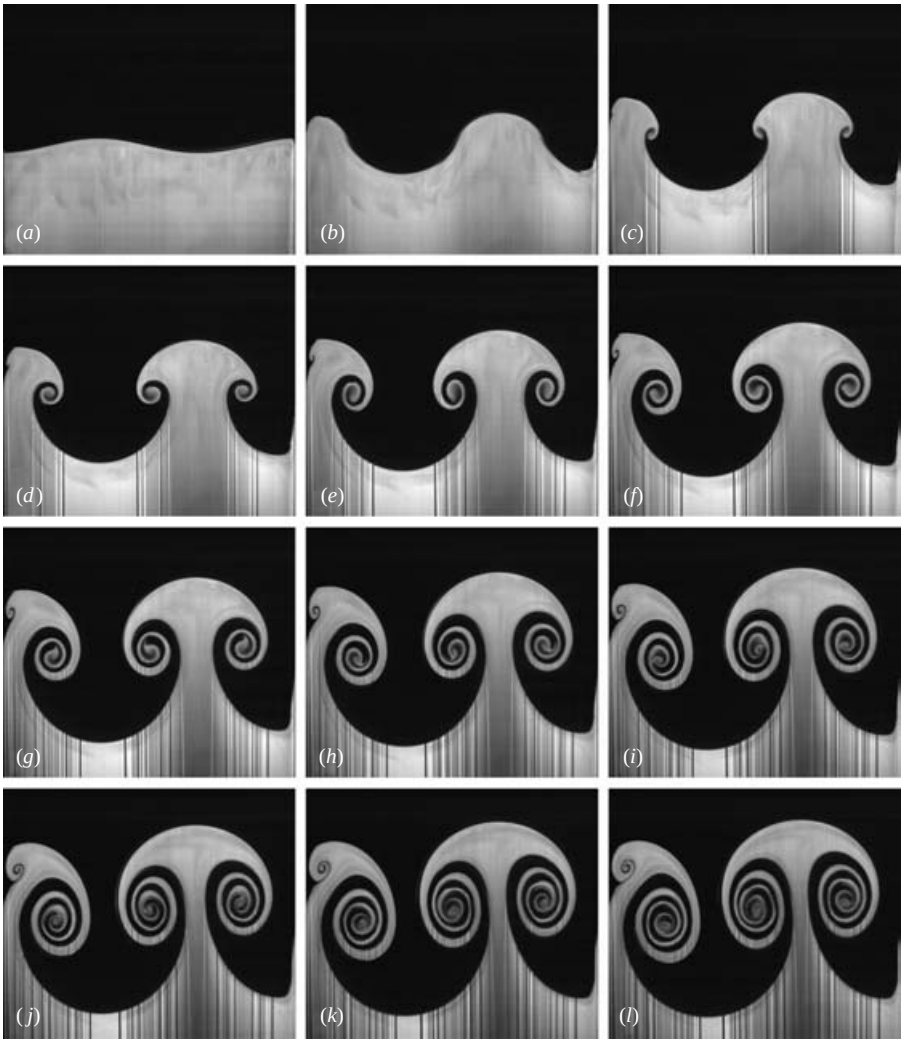

FIGURE 3. A sequence of images from an experiment with $1\frac{1}{2}$ waves and $ka_i = 0.23$. Times relative to the midpoint of spring impact are (*a*) −14 ms, (*b*) 102 ms, (*c*) 186 ms, (*d*) 269 ms, (*e*) 353 ms, (*f*) 436 ms, (*g*) 520 ms, (*h*) 603 ms, (*i*) 686 ms, (*j*) 770 ms, (*k*) 853 ms, (*l*) 903 ms.

experiments is directed from the heavier fluid into the lighter fluid, with the resulting body force on the fluids acting in the downward direction. This orientation causes the initial perturbation to invert (i.e. decrease and pass through zero) before growing in amplitude. Immediately after inversion, the interface retains a sinusoidal shape, but, by figure 3(*b*), the interface begins to become non-sinusodial. Vorticity is deposited along the interface by the baroclinic production mechanism during the acceleration, as given by the two-dimensional vorticity equation:

$$\frac{\mathrm{D}\boldsymbol{\omega}}{\mathrm{D}t} = \frac{1}{\rho}\nabla\rho \times \nabla p. \tag{3}$$

where $\boldsymbol{\omega}$ is the vorticity vector, which is normal to the plane of the two-dimensional motion. In this case, the density gradient $\nabla\rho$ is perpendicular to the interface whereas the pressure gradient ∇p is hydrostatic and thus aligned with the direction of

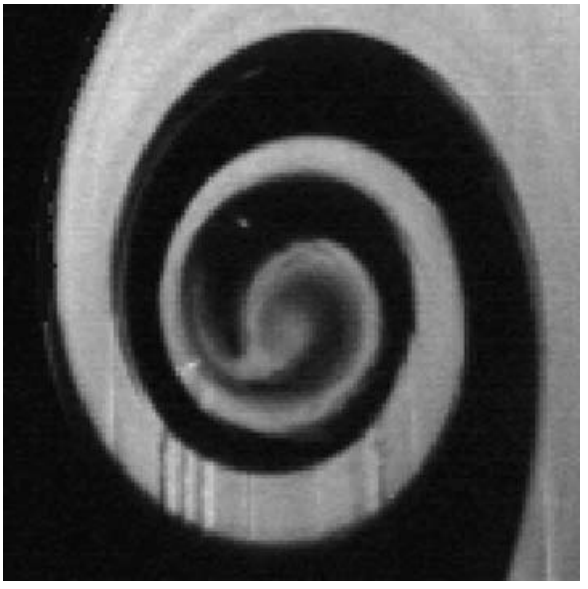

FIGURE 4. A close-up of a vortex core showing the distortion of the vortex tip.

acceleration. The interaction results in a sinusoidal distribution of vorticity. However, as the instability evolves, the vorticity begins to concentrate at points midway between the crests and troughs which correspond to the points of maximum initial interface slope and thus the locations of maximum vorticity (Zabusky 1999). The resulting vortices produce the symmetric mushroom pattern typical of the RT and RM instability.

As time advances, the vortices appear to grow in size as the interface rotates around their centres to form a spiral pattern. The interface is multi-valued by figure 3(*c*), and the vortex centre has completed several turns by figure 3(*l*). As the instability develops, the tips of the vortex spirals evolve into a hammerhead type form, which can be more easily observed in figure 4. As the vortex develops, the inner portion of the tip remains at the vortex centre while the outer half is stretched in length and eventually extends over one full rotation before becoming too fine to observe. Note that the interface retains its top-to-bottom symmetry well into the nonlinear regime. This symmetry is a characteristic of the RM instability with small density differences. Also note that the interface between the two fluids also remains sharp throughout the experiment. The effects of the sidewalls observed in these experiments is small. A thin boundary layer is apparent on the right-hand wall, and a small vortex forms on the left-hand wall.

Figures 5 and 6 show sequences similar to that shown in figure 3 with different perturbation wavelengths. Figure 5 shows the growth of the RM instability with a $\frac{1}{2}$ wave perturbation. Note that, in this case, the final perturbation amplitude in figure 5(*l*) is as large as the $1\frac{1}{2}$ wave case of figure 3. However, the instability itself is not as far developed as the $1\frac{1}{2}$ wave case in that the interface has not yet become double-valued. This difference emphasizes the importance of the non-dimensional amplitude ka, which is still small in the $\frac{1}{2}$ wave case. Figure 6 is a sequence of images from a perturbation with $2\frac{1}{2}$ waves. We can see that in this case the features are

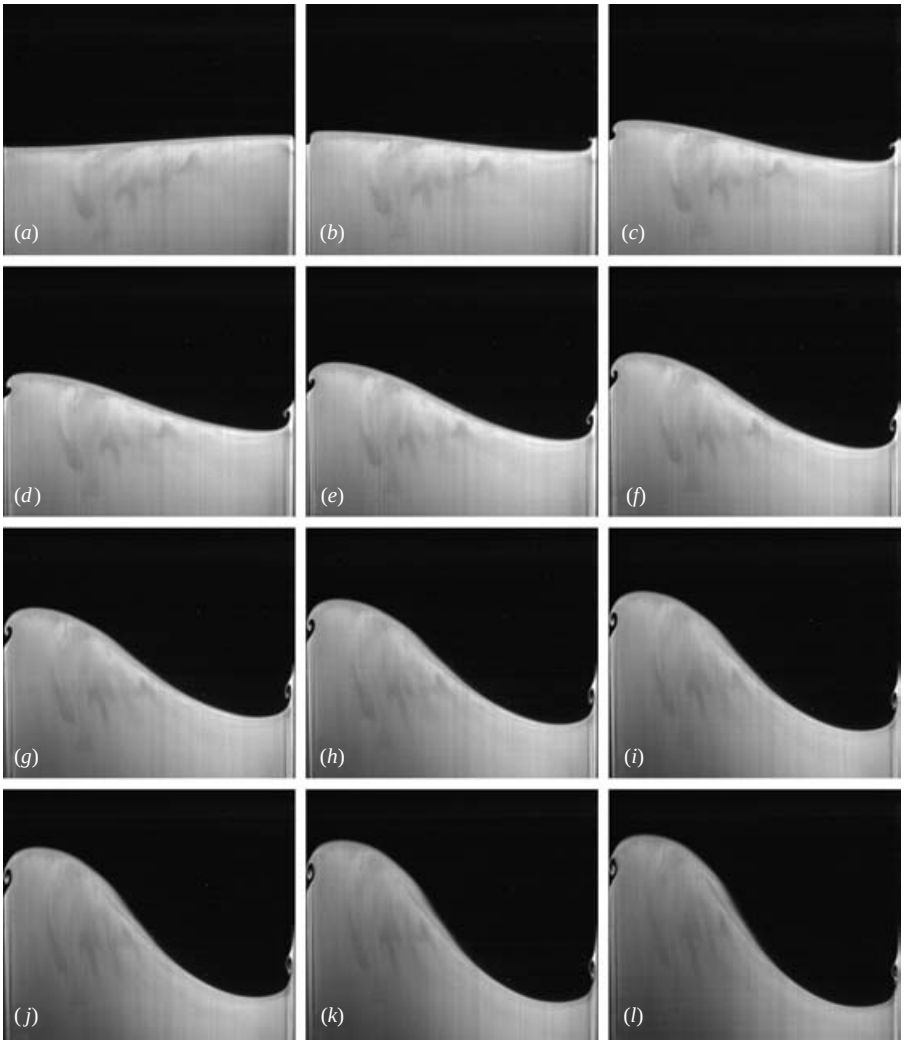

FIGURE 5. A sequence of images from an experiment with $\frac{1}{2}$ wave and $ka_i = 0.06$. Times relative to the midpoint of spring impact are (*a*) −13 ms, (*b*) 120 ms, (*c*) 204 ms, (*d*) 270 ms, (*e*) 354 ms, (*f*) 437 ms, (*g*) 504 ms, (*h*) 587 ms, (*i*) 671 ms, (*j*) 738 ms, (*k*) 821 ms, (*l*) 904 ms.

qualitatively the same as observed in the $1\frac{1}{2}$ wave case. However, as will be discussed later, there are differences in the development of the vortex cores.

3.1. *Linear growth regime*

Richtmyer's (1960) linear stability analysis shows that the amplitude of the interface satisfies the following differential equation:

$$\ddot{a}(t) = -kAg(t)\,a(t). \tag{4}$$

Note that when the gravitational acceleration is zero, as occurs when the sled is in free-fall, the theoretical growth rate $\dot{a}$ is constant. Richtmyer assumed $g(t)$ to be in the form of a Dirac delta function (i.e. $g(t) = \Delta V\,\delta(t)$) and integrated equation (4) to obtain the post-acceleration growth rate in equation (2).

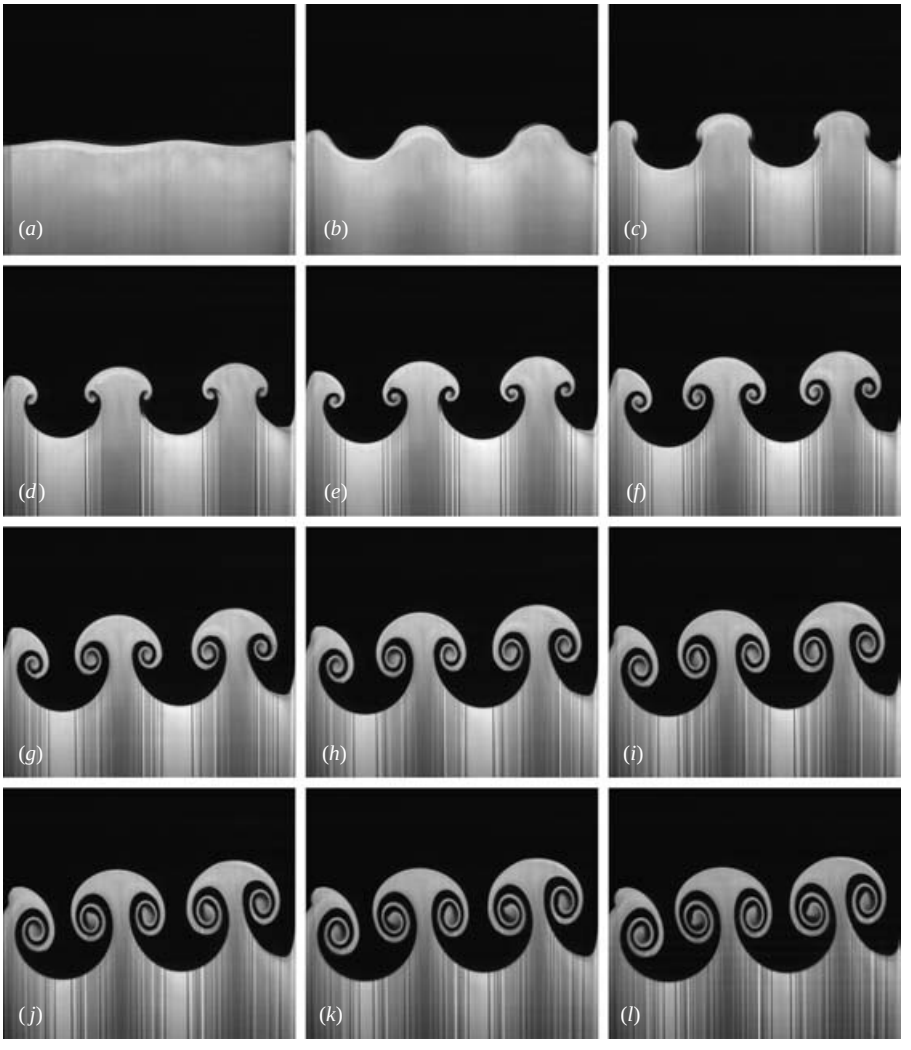

FIGURE 6. A sequence of images from an experiment with $2\frac{1}{2}$ waves and $ka_i = 0.16$. Times relative to the midpoint of spring impact are (*a*) −25 ms, (*b*) 92 ms, (*c*) 175 ms, (*d*) 259 ms, (*e*) 342 ms, (*f*) 426 ms, (*g*) 509 ms, (*h*) 592 ms, (*i*) 676 ms, (*j*) 759 ms, (*k*) 843 ms, and (*l*) 909 ms.

The acceleration pulse imparted to the fluids in the present experiments has a triangular shape as shown in figure 7, with a typical duration of 26 ms, a peak magnitude of $50g$, and an integrated impulse ΔV of $6.4\,\mathrm{m\,s^{-1}}$. The unusual acceleration profile observed in this plot is the result of the impact loading of a stiff spring coupled to the sled by a thick rubber pad. The impact loading of the spring produces a series of compression waves travelling along the length of the spring. Without the rubber pad, these travelling waves would be transmitted to the sled, resulting in a series of large acceleration spikes. The rubber was used to reduce and dampen these oscillations, which are still slightly visible as a higher frequency wave superimposed on the acceleration pulse. The length of this acceleration pulse is too long to use (2) accurately to model the early time instability growth. However, by using the measured perturbation amplitude a and velocity $\dot{a}$ prior to impact,

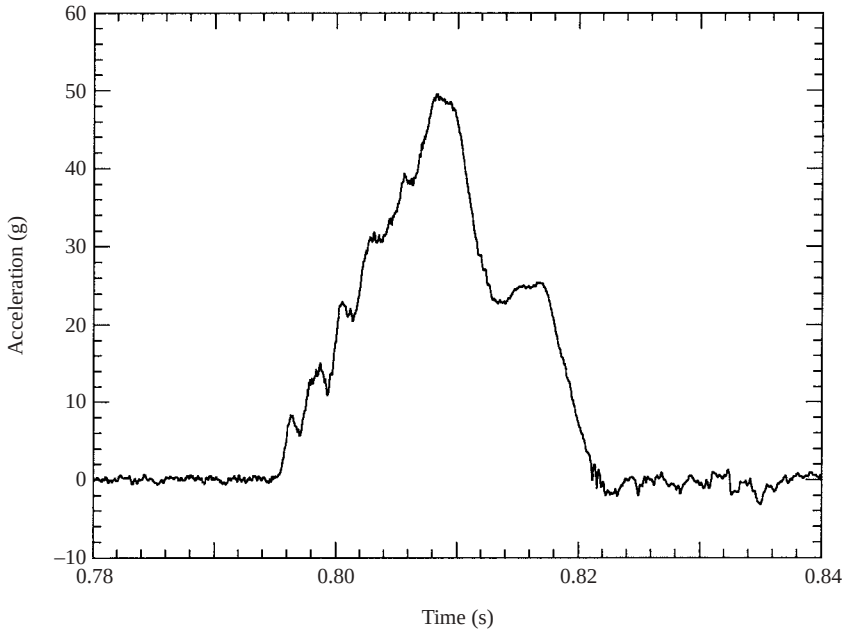

FIGURE 7. A plot of sled acceleration versus time for a typical experiment.

along with the measured acceleration, equation (4) can be numerically integrated to determine the theoretical post-impulse amplitude and velocity. Figure 8 shows the results of this integration for a typical experiment. As described above, the direction of acceleration in these experiments initially results in the temporary stabilization of the interface. Therefore, the amplitude of the crests and troughs decreases while under acceleration. However, the momentum imparted to the fluid by this action remains after the acceleration is removed. Thus, the result is the inversion of the interface, and the subsequent rapid growth of the perturbation.

Figure 9 shows the early time behaviour of the amplitude for all of the single-mode experiments reported here. The amplitude is non-dimensionalized in this plot using the perturbation wavenumber k, while time is non-dimensionalized using the wavenumber and the theoretical initial growth rate $\dot{a}_0$ obtained from the integration of (4). Note that $t = 0$ is found by extrapolating the integrated, theoretical post-impulse perturbation growth to zero amplitude. In this non-dimensionalization, linear theory has a growth rate of 1, and is shown by the solid line in the plot. The experiments show excellent agreement with linear theory up to $k\dot{a}_0 t = 0.3$ and are within 10% of the theory at $k\dot{a}_0 t = 0.7$, where nonlinear effects begin to become important. It should be noted that linear theory is derived assuming $|ka| \ll 1$. Thus, it is surprising how accurate it is at moderate values of ka. The maximum initial amplitudes, ka_i, for the $\frac{1}{2}$ wave, $1\frac{1}{2}$ wave and $2\frac{1}{2}$ wave experiments were 0.06, 0.50 and 0.66, respectively.

3.2. *Weakly nonlinear growth regime*

Figure 10 shows the intermediate-time amplitude measurements ($k\dot{a}_0 t \leqslant 5$), along with lines corresponding to two weakly nonlinear solutions developed by Zhang & Sohn (1997). The first is a weakly nonlinear fourth-order perturbation solution for the amplitude which was developed in much the same manner as Richtmyer's (1960) original linear analysis. Perturbation theory assumes a solution in the form of an

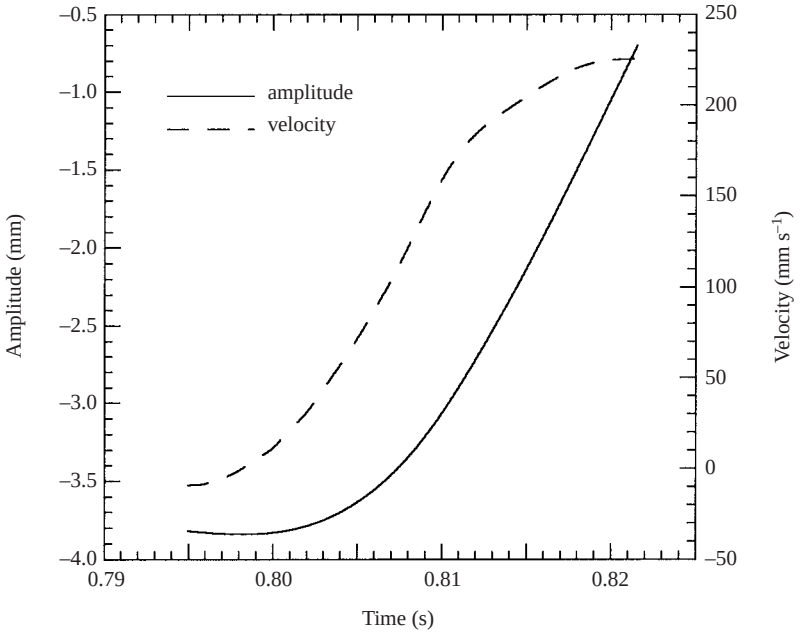

FIGURE 8. A plot of perturbation amplitude and velocity during the impulsive acceleration for a typical experiment obtained from the integration of equation (4) using the measured acceleration history.

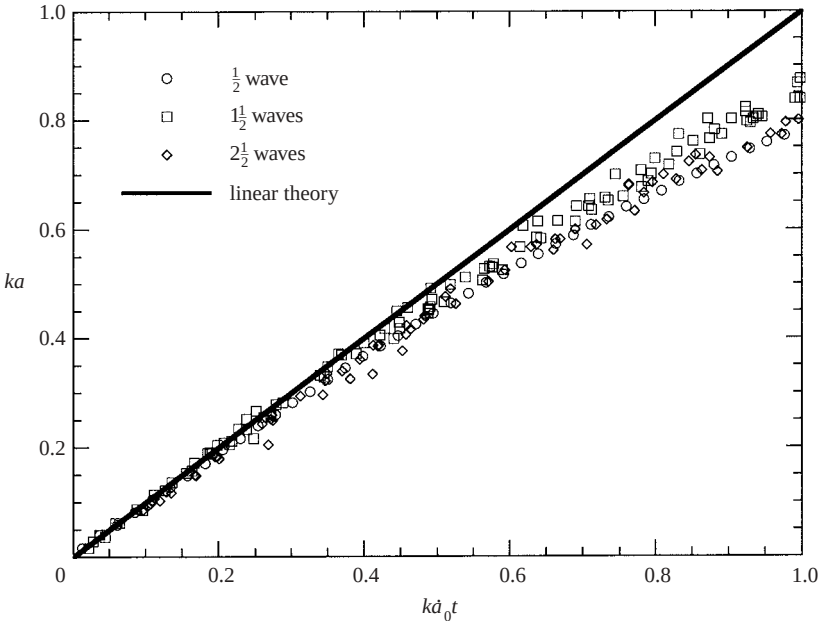

FIGURE 9. A plot of early-time non-dimensional amplitude versus time along with a line corresponding to linear stability theory.

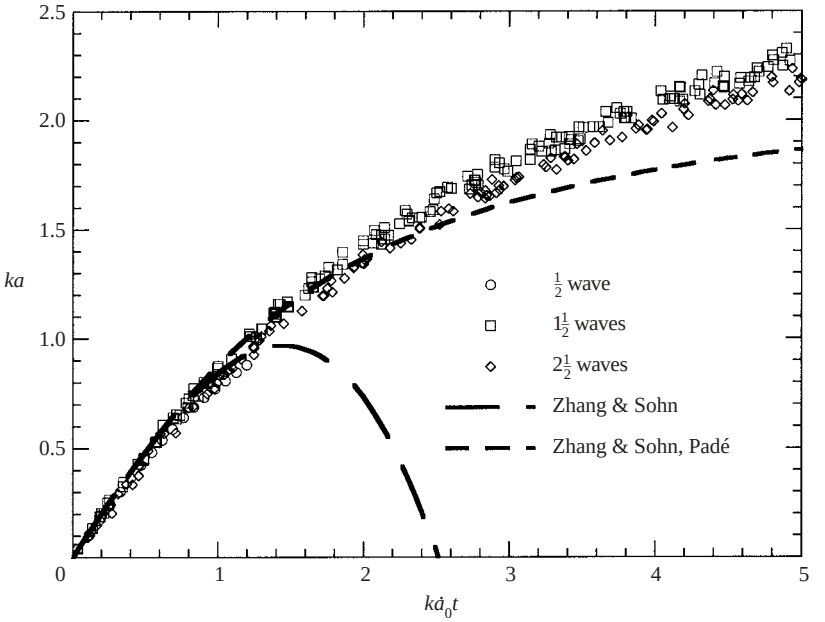

FIGURE 10. A plot of intermediate-time non-dimensional amplitude versus time along with curves corresponding to two weakly nonlinear solutions developed by Zhang & Sohn (1997). Only every third data point in each experiment is shown.

asymptotic expansion for the surface elevation

$$\eta = \eta^{(1)} + \eta^{(2)} + \cdots \tag{5}$$

where $\eta^{(n)} \propto (ka_i)^n$. The solution obtained by Zhang & Sohn assumes an impulsive body force directed from the heavy fluid into the light fluid and a finite initial amplitude. The non-dimensional amplitude ka can be written in terms of the parameters ka_i, A and $\sigma = -k\,A\,\Delta V$. The solution is not directly comparable to the present experiments which have an oppositely directed as well as a finite-duration acceleration. However, by letting the initial amplitude approach zero while maintaining a constant post-impulse growth rate ($ka_i \to 0$ while $\sigma ka_i = \text{constant} = k\dot{a}_0$), we can obtain an expression appropriate for comparison with our experiments. The result for the overall amplitude (the peak-to-peak amplitude divided by two) then becomes

$$ka = k\dot{a}_0 t - \tfrac{1}{6} - \tfrac{1}{3}A^2(k\dot{a}_0 t)^3 + O(k\dot{a}_0 t)^5. \tag{6}$$

Note that the second- and fourth-order terms do not contribute to the overall amplitude. Equation (6) is plotted in figure 10, evaluated at a representative experimental Atwood number of 0.155. This solution agrees with the experimental data to within 10% up to $k\dot{a}_0 t = 1.3$, but then rapidly diverges owing to its cubic form.

Recognizing the limited range of validity of this type of solution, Zhang & Sohn (1997) differentiated their amplitude perturbation expansion to develop a perturbation expansion for the growth rates of the bubble, spike and overall amplitude. A bubble is defined as the portion of the interface where the light fluid penetrates the heavy fluid, and a spike is the portion of the interface where the heavy fluid penetrates the light fluid. The overall amplitude is the average of the bubble and spike amplitudes. These series solutions were then approximated with Padé approximants to extend their range of validity. By again taking the limit as $ka_i \to 0$ while keeping

$\sigma k a_i = \text{constant} = k\dot{a}_0$, Zhang & Sohn's expression for the overall amplitude growth rate can be rewritten (for the case when $ka_i > A^2 - 1/2$) as

$$k\dot{a} = \frac{k\dot{a}_0}{1 + \left(\frac{1}{2} - A^2\right)(k\dot{a}_0 t)^2}, \tag{7}$$

which after integration yields:

$$ka = \frac{1}{\sqrt{\frac{1}{2} - A^2}} \tan^{-1}\left(\sqrt{\tfrac{1}{2} - A^2}\, k\dot{a}_0 t\right). \tag{8}$$

Evaluating (8), using $A = 0.155$, results in the curve shown in figure 10. This expression extends the range of agreement (to within 10%) for this theory to $k\dot{a}_0 t = 3$.

3.3. *Fully nonlinear growth regime*

3.3.1. *Vortex model*

Jacobs & Sheeley (1996) noted that the vorticity in these experiments eventually coalesces into discrete vortices. They subsequently modelled the flow as a row of line vortices of alternating sign, assuming an Atwood number of zero and obtained the following expression for the overall amplitude

$$ka = \sinh^{-1}\left(\frac{2}{\pi} k\dot{a}_0 (t - t_p) + \sinh(ka_p)\right), \tag{9}$$

where t_p and a_p are the time and amplitude, respectfully, when the vorticity is assumed to concentrate. Since $\sinh^{-1}(x) \cong \ln(2x)$ for large values of x, this model gives logarithmic late time growth. Thus, the late time velocity becomes

$$\dot{a} = \frac{1}{k\,t}. \tag{10}$$

Figure 11 is a logarithmic plot of the late-time velocity calculated by taking the derivative (using a first-order backward difference) of the amplitude measurements for $k\dot{a}_0 t \leqslant 30$. These measurements are shown normalized by the theoretical initial growth rate $\dot{a}_0$ obtained from the integration of (4). As is clearly observed in this plot, the velocity agrees very well with equation (11) for $k\dot{a}_0 t \approx 2$, although the logarithmic coordinates make it insensitive to detecting small differences in the constant of proportionality in equation (10). The increased scatter at late times is due in part to the decreasing resolution in the derivative of the amplitude at late times.

Figure 12 compares the late-time amplitude measurements ($k\dot{a}_0 t \leqslant 30$) with a curve generated from (9) assuming the vorticity concentrates immediately after impact, i.e. $k\dot{a}_0 t_p = 0$. The vortex model gives an initial growth rate that is lower by a factor of $\pi/2$ than that given by linear theory. This is consistent with the assumption in the linear stability analysis that the vorticity has a sinusoidal distribution, rather than a discrete distribution assumed by the vortex model. However, since the vorticity in the experiments does not concentrate until much later, this curve underestimates the amplitude. Thus, the condition $k\dot{a}_0 t_p = 0$ can be considered a lower bound on the amplitude. Nevertheless, the curve appears to have the same general shape as the experimental data, and differs from the measurements by less than 10% at late times. Also shown in figure 12 is a curve generated assuming the vorticity concentrates at $k\dot{a}_0 t_p = 6$ ($ka_p = 2.4$), at a point approximately corresponding to figure 3(f) and figure 6(g). This assumption reduces the difference between the model and the late-time

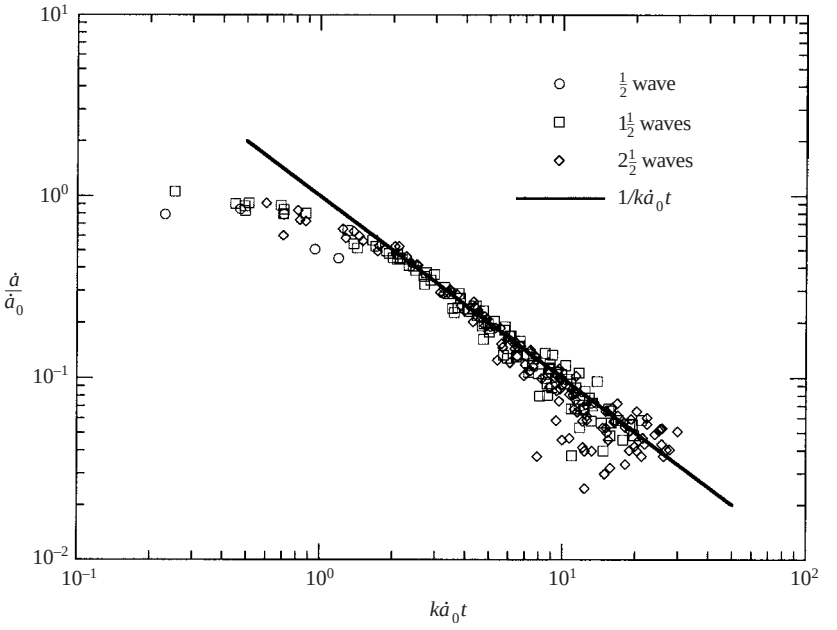

FIGURE 11. A plot of late-time non-dimensional velocity versus time compared with the asymptotic value given by the vortex model (10). Every tenth data point in each experiment is shown.

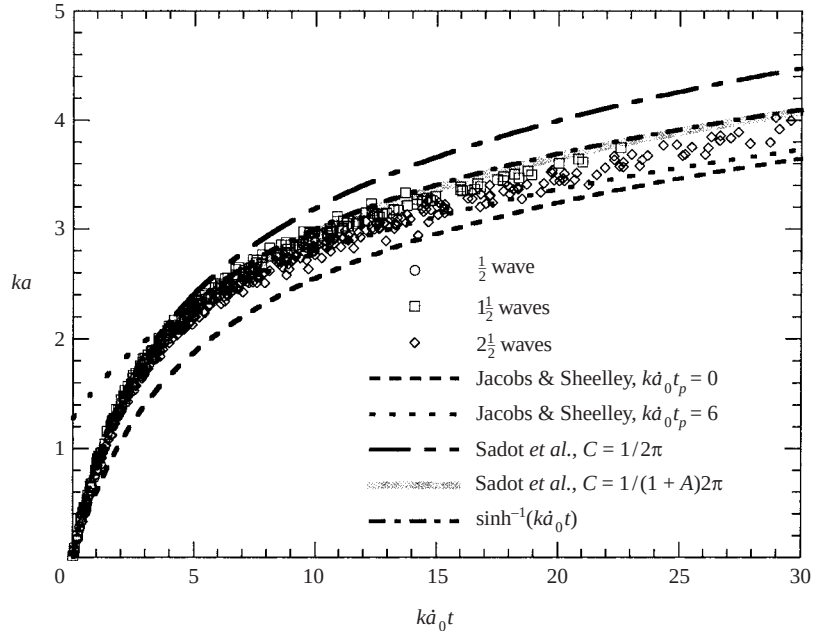

FIGURE 12. A plot of late-time non-dimensional amplitude versus time along with curves from several nonlinear models. Every fifth data point in each experiment is shown.

amplitude to less than 5% over the range tested. This difference may be attributed to the fact that the model is strictly valid only for Atwood number of 0. It is interesting to note that increasing the initial growth rate in (9) by a factor of $\pi/2$ yields, $ka = \sinh^{-1}(k\dot{a}_0 t)$, which has the same functional form as (9), but also captures the correct initial growth rate. This function is also plotted in figure 12 showing that even though it assumes an incorrect value of the circulation, it provides an excellent fit to the data.

3.3.2. *Interpolation model*

Sadot *et al.* (1998) proposed the following rational function interpolation between existing early-time and late-time models for the bubble and spike velocities:

$$U_{b/s}(t) = U_0 \frac{1 + Bt}{1 + Dt + Et^2}, \tag{11}$$

where

$$B_{b/s} = U_0 k, \tag{12}$$

$$D_{b/s} = (1 \pm A) U_0 k, \tag{13}$$

$$E_{b/s} = \frac{1 \pm A}{1 + A} \frac{1}{2\pi C} U_0^2 k^2. \tag{14}$$

and U_0 is the initial velocity (i.e. $\dot{a}_0$). In these expressions, the plus sign is used for the bubble velocity and the minus sign is used for the spike velocity. At small time, the bubble and spike velocities are given by:

$$U_{b/s} = U_0 (1 \mp A k U_0 t). \tag{15}$$

which is identical to the first two terms of the fourth-order weakly nonlinear perturbation solution of Zhang & Sohn (1997). At large time, the bubble and spike velocities are given by:

$$U_{b/s} = \frac{2\pi C (1 + A)}{k (1 \pm A) t}. \tag{16}$$

Thus, they possess the $1/t$ dependence of the vortex model discussed above. The constant C is a function of the asymptotic velocity of the bubbles and spikes. The values for C given by Sadot *et al.* (1998) are obtained from the computations of Alon *et al.* (1995), in which they found $C = 1/3\pi$ for $A \geqslant 0.5$, and $1/2\pi$ for $A \to 0$. However, these values can also be obtained using methods similar to those used by Takabe & Yamamoto (1991) and Alon *et al.* (1995) to model the motion of an RT bubble. The differential equation governing the motion of a two-dimensional bubble in a gravitational field (see figure 13) is:

$$(\rho_1 + \kappa \rho_2) V_b \frac{\partial U_b}{\partial t} = -\tfrac{1}{2} C_D S_b \rho_2 U_b^2 + (\rho_2 - \rho_1) V_b g, \tag{17}$$

where V_b is the bubble volume, S_b is the bubble frontal area, C_D is the bubble drag coefficient, and κ is the virtual mass coefficient. The densities of the light and heavy fluids are ρ_1 and ρ_2, respectively. Equation (17) is a simple force balance with acceleration, drag and buoyancy terms. In the case of RM instability in the post-impulse stage, the acceleration $g = 0$. Thus, if $\kappa = 1$ as would be the case if the bubble had the shape of a circular cylinder, and it is assumed that $V_b/S_b \propto \lambda \propto 1/k$, the

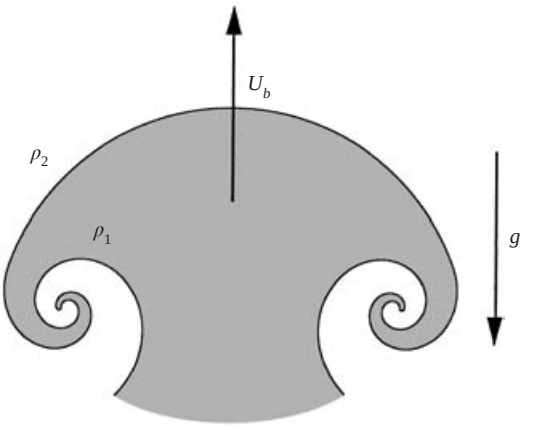

FIGURE 13. The configuration used for the bubble force balance model.

solution for the bubble velocity is:

$$U_b \propto \frac{1}{k\,(1+A)\,t}. \tag{18}$$

This same procedure can be used for an RM spike, employing a slightly modified form of (17), yielding:

$$U_s \propto \frac{1}{k\,(1-A)\,t}. \tag{19}$$

Note that equation (10), developed using the vortex model with $A=0$, yields the asymptotic velocity $U = 1/kt$ for both the bubble and the spike. Therefore, the constant of proportionality in (18) and (19) may reasonably be assumed to be 1 for both the bubble and the spike in the small Atwood number limit. Also note that equation (19) for the spike velocity does not apply when $A=1$, in which case the drag is theoretically zero and the solution to the force balance differential equation (17) has a different form. Equations (18) and (19) can be used with equation (16) (with the proportionality constant $=1$) to solve for C, yielding:

$$C = \frac{1}{(1+A)2\pi}. \tag{20}$$

This constant C is equal to $1/3\pi$ at $A=0.5$ and $1/2\pi$ at $A=0$. Thus, it is in agreement with the computational results in Alon *et al.* (1995) in this range of Atwood numbers. However, it should be noted that (20) yields a value $C=1/4\pi$ in the limit $A \to 1$ which disagrees with previous numerical and theoretical studies which give $C=1/3\pi$ (Hecht, Alon & Shvarts 1994; Alon *et al.* 1995). This difference implies that the constant of proportionality in (18) and (19) may be only 1 for small or moderate values of the Atwood number. Note that Alon *et al.* report using the same analytical procedure as described above, but obtained different expressions for the asymptotic velocities (equations (18) and (19)). This discrepancy was later corrected by Oron *et al.* (2001). However, this more recent analysis uses a much larger value for the added mass coefficient. Thus, they obtain expressions for $U_{b/s}$ that differ significantly in form from ours.

The perturbation amplitude can be obtained from (11) by integrating the bubble and spike velocities separately. The result of this integration for the overall amplitude

(the average of the bubble and spike amplitudes) is plotted on figure 12 for $C = 1/2\pi$. The curve shows good agreement with the early-time data, but overestimates the late-time amplitude by 10%. Also shown on figure 12 is a curve generated by integrating equation (11) using $C = 1/(1 + A)2\pi$ with the experimental value of $A = 0.155$. This curve appears to model the initial growth rate correctly, as well as the late-time asymptotic velocity. This modified form of Sadot *et al.*'s model shows much better agreement with the late-time amplitude measurements and appears to predict the perturbation amplitude data accurately over the entire time duration investigated. The improved agreement with the modified form of this model can be attributed to the fact that the value $C = 1/2\pi$ is strictly true only for Atwood number zero. Note that Alon *et al.* acknowledged that C varied with Atwood number, but did not give a specific function for Atwood numbers less than 0.5. It should be stressed that this model does not intrinsically solve the flow field, but is simply an interpolation that matches both the early-time and late-time growth rates.

3.3.3. *Bubble and spike measurements*

The overall amplitude measurements presented in the previous sections ignore differences between the bubble and spike amplitudes. As the Atwood number of the system approaches zero, the bubbles and spikes become symmetrical about the mean interface location. Thus, the bubbles and spikes have identical amplitudes, growth rates, and shapes. However, at larger Atwood numbers, differences between the bubbles and spikes become apparent. The heavier spikes grow faster than the lighter bubbles. The spikes also have smaller widths than the bubbles. In the experiments presented here with Atwood number of 0.155, there is a small but measurable difference between the bubble and spike amplitudes.

Figure 14 shows the separate bubble and spike amplitudes for the experiments. The amplitude is measured relative to the location of the flat interface prior to impact. The growth rates of the bubbles and spikes are initially the same, as predicted by weakly nonlinear theory. However, the spike amplitude becomes 10% greater than the bubble amplitude when $k\dot{a}_0 t = 0.8$, and 30% greater when $k\dot{a}_0 t = 15$. Also shown on figure 14 are curves corresponding to the bubble and spike amplitudes found by integrating (11). These results use our derived constant C (equation (20)) that more accurately models the late-time growth rate. Again, this modified model shows good agreement with the experimental measurements. However, experiments at other Atwood numbers would be necessary to determine whether the expression has the correct Atwood number dependence.

3.4. *Multi-mode initial perturbations*

While single-mode perturbations are the most often studied in laboratory experiments, real applications involving RM instability are inevitably composed of disturbances with many wavelengths. Multi-mode interfacial perturbations were generated in the present investigation by oscillating the fluid container with a combination of two or more different frequencies. Figure 15 is a sequence of images showing the evolution of an experiment initiated with a combination of a $1\frac{1}{2}$ wave mode and a $2\frac{1}{2}$ wave mode as the initial perturbation. Figure 15(*a*) was taken slightly before the impulsive acceleration and shows the initial interface shape resulting from the combination of these two modes. According to linear theory, at small amplitudes, the two modes evolve independently and the mode with the shorter wavelength grows more rapidly (since $\dot{a} \propto ka_i$). In figure 15(*b*), the long wavelength mode has decreased to nearly zero amplitude, while the short wavelength mode has inverted and thus is the dominant

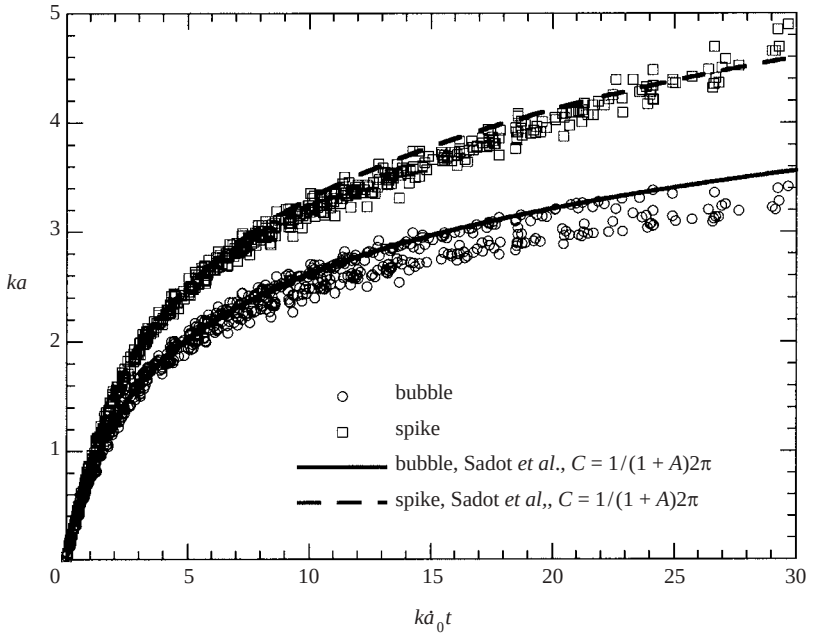

FIGURE 14. A plot of separate bubble and spike amplitudes versus time compared with the model of Sadot *et al.* with modified constant C. Every fifth data point in each experiment is shown.

mode visible. In figures 15(*c*)–15(*l*), this multi-mode instability evolves, forming a more complex structure than that observed in the small-amplitude single-mode experiments. Note that the vorticity concentrates at points where the initial perturbation has local maxima in slope, which are also the points of maximum baroclinic vorticity generation. Also note the unusual symmetry of the interface about the centre of the tank owing to the small density difference of the fluids.

3.4.1. *Multi-mode analysis*

To analyse the multi-mode experiments, the interface was parameterized by finding the coordinates of a set of points (x_I, y_I) lying on the interface using an edge-detection routine, neglecting points near the sides of the tank to reduce the possible wall effects. These points were then curve-fitted to a function of the form,

$$y(x) = y_0 + a_1 \sin[k_1(x - x_0)] + a_2 \sin[k_2(x - x_0)] + \cdots \tag{21}$$

to determine the individual mode amplitudes, assuming k_1 and k_2 to be equal to those of the imposed initial perturbation. An example of the resulting curve fit is shown in figure 16, which illustrates the capability of the perturbation generation method to produce high-fidelity multi-mode initial perturbations. As mentioned above, at small amplitudes the various modes should act independently of each other and their evolution should be described by linear theory. Therefore, the method of analysis used for the single-mode experiments was also employed for the multi-mode experiments. Figure 17 shows the time dependence of the non-dimensional mode amplitude for nine multi-mode experiments. The modes show excellent agreement with linear theory for $k\dot{a}_0 t < 0.3$. Beyond that time, the interface becomes multi-valued (at different times depending on the initial conditions) making the curve fitting of (21) no longer valid. The agreement between the measurements and theory at early times in the plot

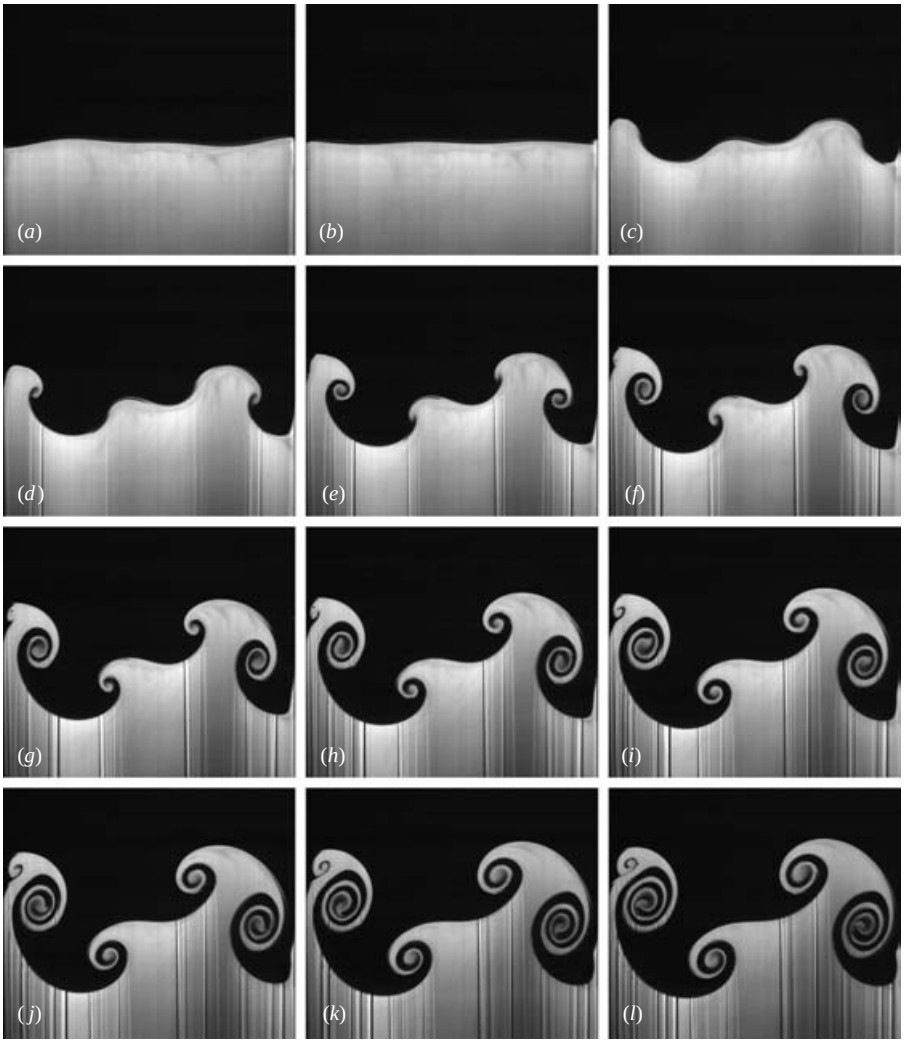

FIGURE 15. A sequence of images from a multi-mode experiment with a combination of a $1\frac{1}{2}$ wave and a $2\frac{1}{2}$ wave initial perturbation. Times relative to the midpoint of spring impact are (*a*) −15 ms, (*b*) 18 ms, (*c*) 101 ms, (*d*) 185 ms, (*e*) 285 ms, (*f*) 368 ms, (*g*) 452 ms, (*h*) 552 ms, (*i*) 635 ms, (*j*) 719 ms, (*k*) 819 ms, (*l*) 902 ms.

confirms that the multi-mode perturbations do act independently and follow linear theory in the small-amplitude regime.

3.4.2. *Multi-mode examples*

Other examples of multi-mode RM instabilities are shown in figures 18–20. Figure 18 shows the RM instability resulting from the combination of a $\frac{1}{2}$ wave and $2\frac{1}{2}$ wave initial perturbation. The two different wavelengths are clearly present in figure 18(*a*), taken before the impulsive acceleration. This initial perturbation produces three vortices of the same sign with the centre vortex larger in size. The development of an initial perturbation with $1\frac{1}{2}$ waves and $4\frac{1}{2}$ waves is shown in figure 19. Note that the $4\frac{1}{2}$ wave mode is the second harmonic of the $1\frac{1}{2}$ wave mode. Thus, it produces two

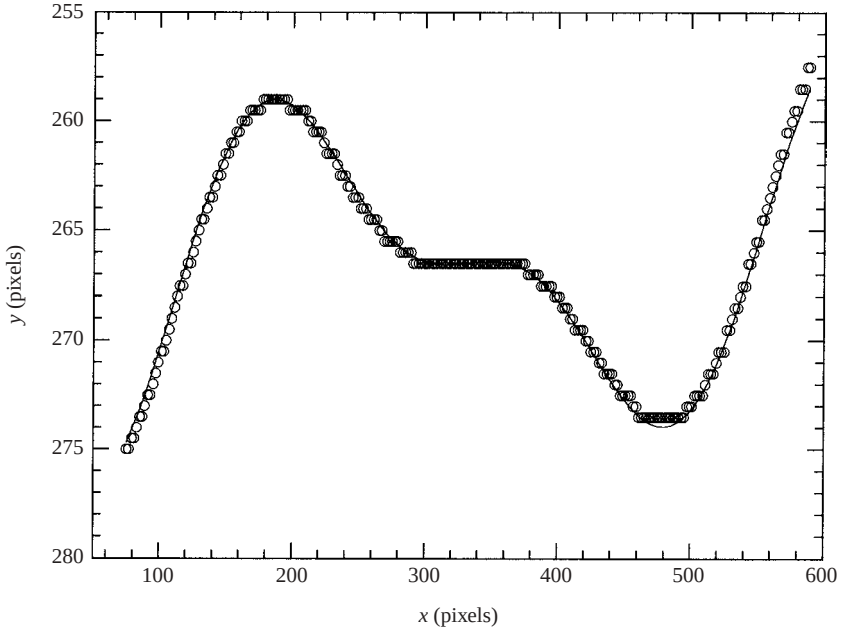

FIGURE 16. A plot showing the curve fit of (21) to the interface locations obtained from an edge-detected image from an experiment with a combination of $1\frac{1}{2}$ and $2\frac{1}{2}$ waves.

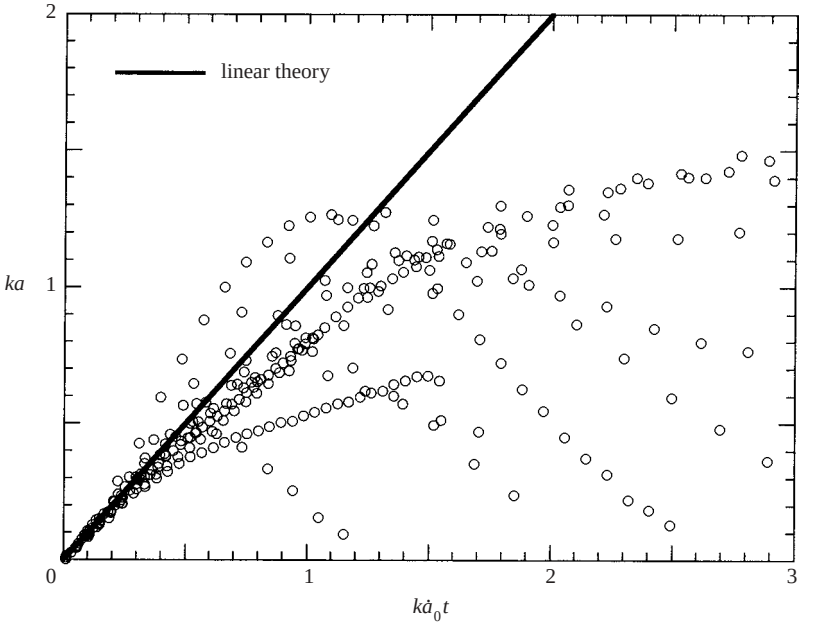

FIGURE 17. A plot of non-dimensional amplitude versus time for nine multi-mode experiments with 19 total modes. Mode combinations include: $\frac{1}{2}$ & $2\frac{1}{2}$; $\frac{1}{2}$ & $4\frac{1}{2}$; $1\frac{1}{2}$ & $2\frac{1}{2}$; $1\frac{1}{2}$ & $4\frac{1}{2}$; $1\frac{1}{2}$, $3\frac{1}{2}$ & $4\frac{1}{2}$; $2\frac{1}{2}$ & $4\frac{1}{2}$.

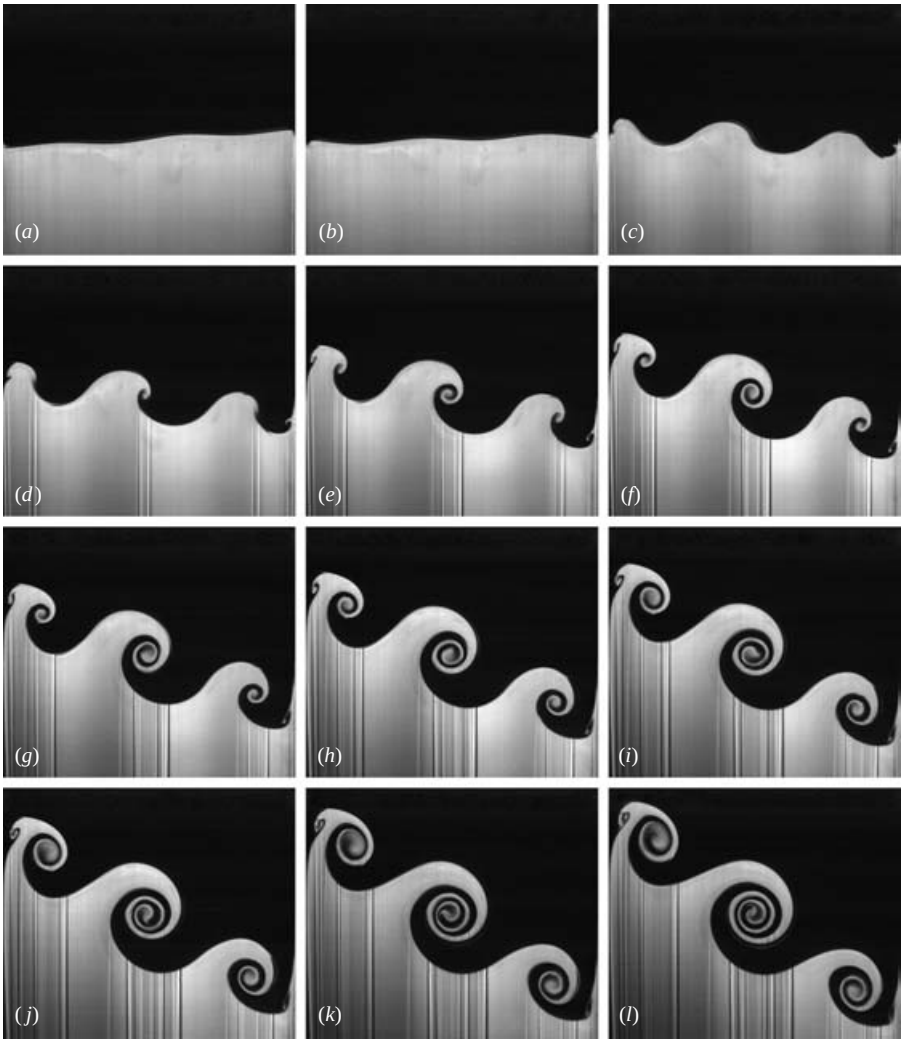

FIGURE 18. A sequence of images from a multi-mode experiment with a combination of a $\frac{1}{2}$ wave and a $2\frac{1}{2}$ wave initial perturbation. Times relative to the midpoint of spring impact are (*a*) −27 ms, (*b*) 23 ms, (*c*) 107 ms, (*d*) 190 ms, (*e*) 290 ms, (*f*) 374 ms, (*g*) 457 ms, (*h*) 557 ms, (*i*) 641 ms, (*j*) 724 ms, (*k*) 824 ms, (l) 907 ms.

vortices per fundamental half wavelength in contrast to one vortex per half wavelength produced in the single-mode experiments. This mode combination evolves to form a double-mushroom shape with vertically stacked vortices. The detailed development of this and all multi-mode experiments depended strongly on the relative amplitudes of the initial modes.

Figure 20 shows the RM instability produced by a $\frac{1}{2}$ wave and $4\frac{1}{2}$ wave initial perturbation. Five vortices of the same sign are formed over the half wavelength of the fundamental perturbation. The central three vortices appear to be the same strength, thus this flow closely resembles Kelvin–Helmholtz instability. Figure 20(*a*) shows that the amplitude of the $\frac{1}{2}$ wave perturbation is much larger than that of the $4\frac{1}{2}$ wave perturbation. The large $\frac{1}{2}$ wave perturbation produces a shear flow across

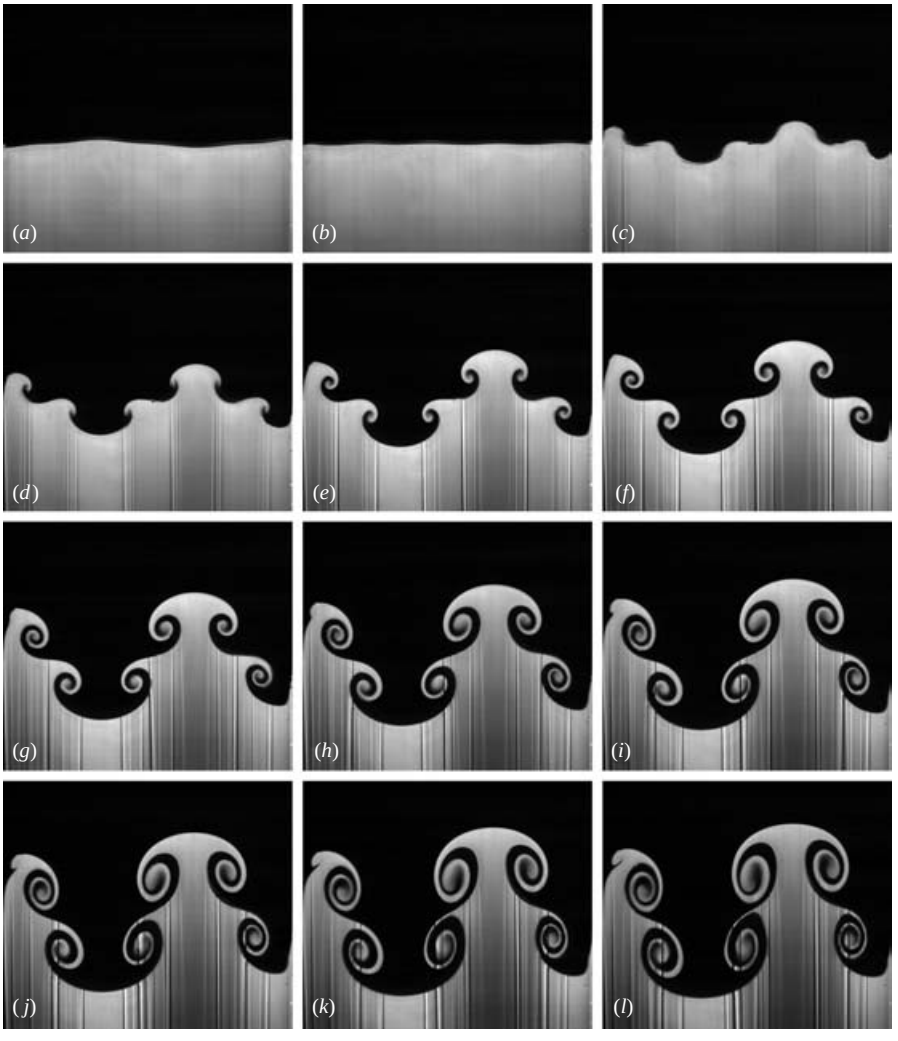

FIGURE 19. A sequence of images from a multi-mode experiment with a combination of a $1\frac{1}{2}$ wave and a $4\frac{1}{2}$ wave initial perturbation. Times relative to the midpoint of spring impact are (*a*) −18 ms, (*b*) 16 ms, (*c*) 99 ms, (*d*) 182 ms, (*e*) 282 ms, (*f*) 366 ms, (*g*) 449 ms, (*h*) 549 ms, (*i*) 633 ms, (*j*) 716 ms, (*k*) 816 ms, (*l*) 900 ms.

the tank, with the small $4\frac{1}{2}$ wave perturbation serving as an initial perturbation for the Kelvin–Helmholtz instability.

3.5. *Reynolds number effects*

3.5.1. *Reynolds number definition*

An important aspect of RM instability that has not been discussed in earlier investigations is the dependence of the Reynolds number on the flow. The Reynolds number is defined as $Re = Ul/\nu$, where U, l and ν are characteristic values of velocity, length and kinematic viscosity. Obvious length and velocity scales appropriate in RM

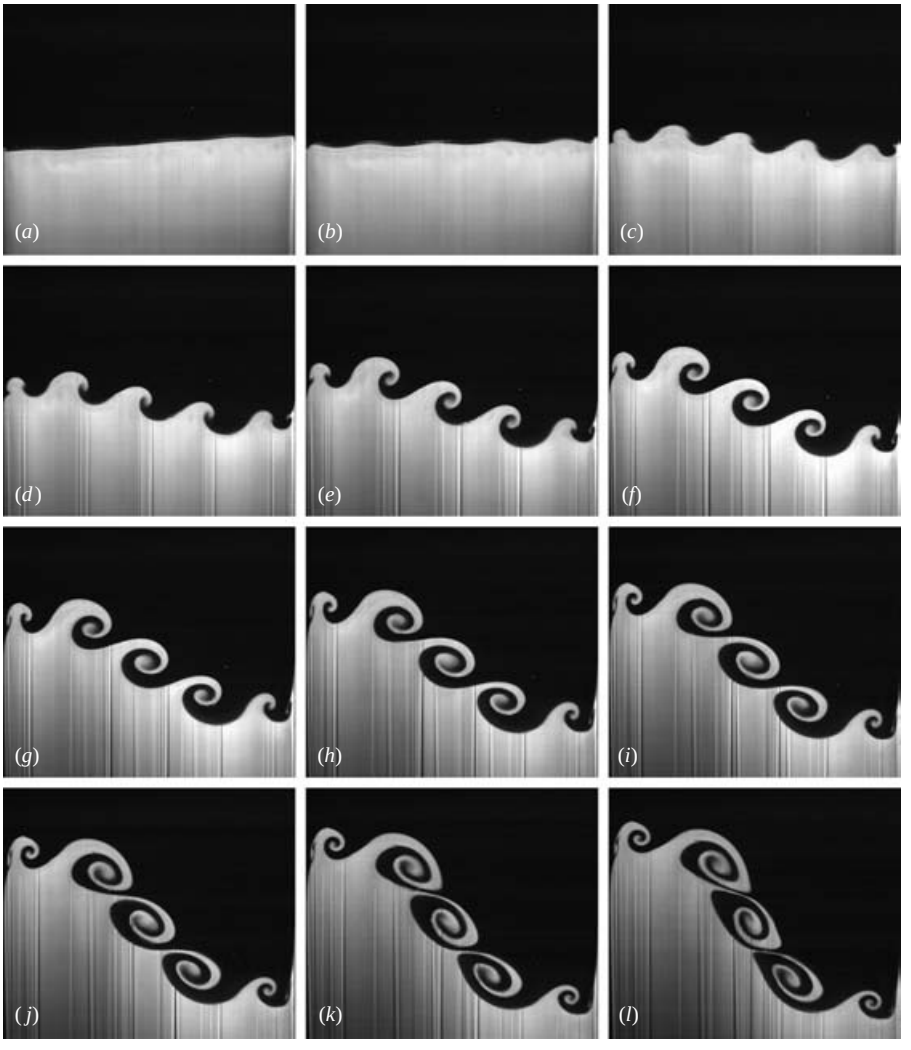

FIGURE 20. A sequence of images from a multi-mode experiment with a combination of a $\frac{1}{2}$ wave and a $4\frac{1}{2}$ wave initial perturbation. Times relative to the midpoint of spring impact are (*a*) −20 ms, (*b*) 30 ms, (*c*) 113 ms, (*d*) 197 ms, (*e*) 297 ms, (*f*) 380 ms, (*g*) 464 ms, (*h*) 564 ms, (*i*) 647 ms, (*j*) 731 ms, (*k*) 831 ms, (*l*) 914 ms.

instability are the perturbation amplitude a and growth rate $\dot{a}$, yielding

$$Re_p = \frac{a\dot{a}}{(\nu_1 + \nu_2)/2}. \tag{22}$$

Figure 21 shows a plot of Reynolds number defined using (22) for a typical single-mode experiment from this investigation which shows that (22) yields a time dependent value. Thus, defined this way, the Reynolds number initially grows linearly in time (as is indicated by linear theory) peaking at $k\dot{a}_0 t = 1.6$ and then decays toward zero. It is important to recognize that the flow at late time is dominated by the vortices that form at the nodes of the perturbation. Thus, an alternative Reynolds number more appropriate to the vortical flow may be defined using the circulation of one of

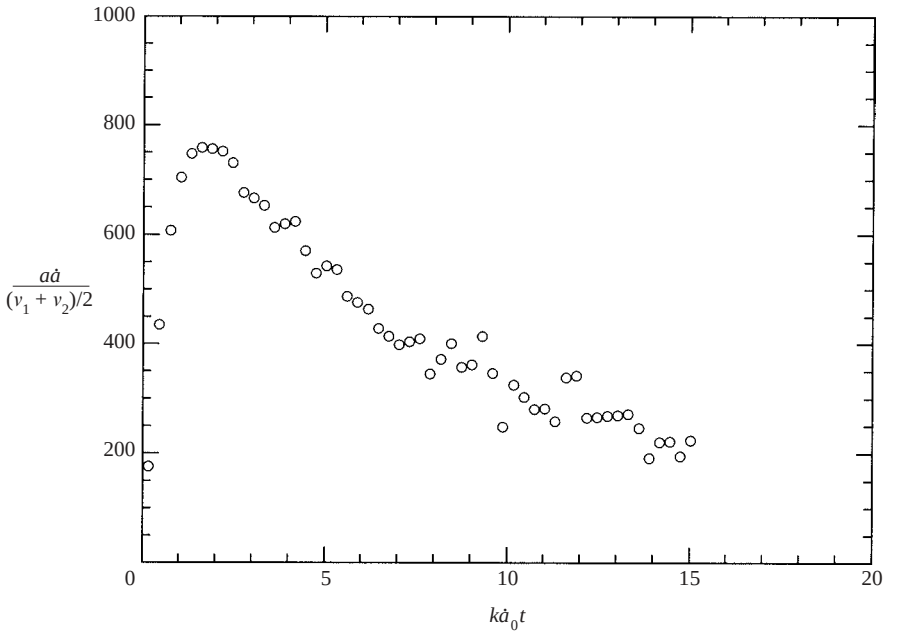

FIGURE 21. A plot of perturbation Reynolds number (based on amplitude and velocity) versus time for a typical experiment.

the vortices and the average kinematic viscosity of the two fluids:

$$Re = \frac{\Gamma}{(\nu_1 + \nu_2)/2}. \tag{23}$$

Note that the circulation cannot be easily measured in the present experiments. However, it can be estimated from measurements of the initial growth rate, as was done by Jacobs & Sheeley (1996). If we assume the flow field to be that given by linear stability theory, the circulation can be found by integrating the vortex sheet strength over half a wavelength of the interface. The result is that the circulation strength of a vortex is given by:

$$\Gamma = \frac{4\dot{a}_0}{k}, \tag{24}$$

which is constant during the experiment if viscous dissipation and the baroclinic generation of secondary vorticity is negligible. Therefore, the vortex Reynolds number can be calculated using:

$$Re = \frac{8\dot{a}_0}{k(\nu_1 + \nu_2)}. \tag{25}$$

Thus, this definition yields a Reynolds number that has a constant value. This vortex Reynolds number (Re_v) can be related to the perturbation Reynolds number (Re_p). Figures 9, 11 and 12 demonstrate that the dimensionless amplitude ka in the experiments is a function of only the dimensionless time scale $k\dot{a}_0 t$, i.e.

$$ka = f(k\dot{a}_0 t), \tag{26}$$

therefore

$$k\dot{a} = k\dot{a}_0 f'(k\dot{a}_0 t), \tag{27}$$

and the perturbation Reynolds number can be written as

$$\begin{aligned} Re &= \frac{a\dot{a}}{(\nu_1+\nu_2)/2} \\ &= \frac{1}{k^2}\frac{2ka\dot{k}\dot{a}}{\nu_1+\nu_2} \\ &= \frac{2\dot{a}_0}{k(\nu_1+\nu_2)}ff' \\ &= Re_v\frac{ff'}{4}. \end{aligned} \tag{28}$$

Therefore, the perturbation Reynolds number is equal to the vortex Reynolds number multiplied by a function of time, the value of which ranges from 0 to 0.16. This vortex Reynolds number is also proportional to the Reynolds number defined using initial growth rate and perturbation wavelength as velocity and length scales. Unless specifically noted, values of the Reynolds number quoted in the following text refer to the vortex Reynolds number (23). Note that the value of Reynolds number achievable in an experiment varies greatly with the perturbation wavelength. Thus, it is possible to achieve much larger values of circulation and Reynolds number using longer wavelength perturbations. The Reynolds number for the experiments presented here range from 1100 to 8500.

3.5.2. *Vortex turning rate*

The experiments in this study spanned a wide range of initial amplitudes and Reynolds numbers. It is therefore remarkable that the non-dimensional scaling used in figures 9, 11 and 12 effectively collapses the amplitude measurements for the entire range of experimental parameters investigated. This degree of collapse indicates that the late-time amplitude is determined only by the perturbation wavenumber and initial growth rate. Thus, the Reynolds number does not appear to influence the amplitude measurements. However, the Reynolds number was observed in the experiments to have an effect on the evolution of the vortex cores. This effect can be observed by visually comparing the images in figures 3 and 6. In the last few images of both of these sequences, the non-dimensional amplitude is approximately the same. However, we can easily observe a noticeable difference in the vortex cores, in which the longer wavelength experiment shows a significant increase in the number of turns or coils. This effect can be quantified by considering the vortex core turning rate (i.e. the rate of rotation of the vortex cores). One method of quantifying the turning rate is to determine the non-dimensional time when the interface becomes multi-valued and when the centre of the vortex completes a specified number of turns. Figure 22 shows measurements of the time when the interface first becomes multi-valued and when the vortex core has completed 1, 2 and 3 turns plotted as a function of the Reynolds number. The interface is considered multi-valued when its maximum slope becomes infinite, i.e. when it has rotated 90° from a horizontal position. Defining the number of turns is more difficult and subjective in part because of the non-symmetrical form and rapid rate of the initial vortex development. After attaining infinite slope, the interface in a small region near the vortex core rapidly rotates 180° and develops a fold that eventually becomes the tip of the vortex spiral. For consistency, this folded condition is considered to be the starting point in the rotation process. Turning is then defined as the angular rotation of this heavy (dyed) fluid tip. A completed turn is defined as when the heavy fluid tip of the spiral is vertical and has rotated $n \times 360°$

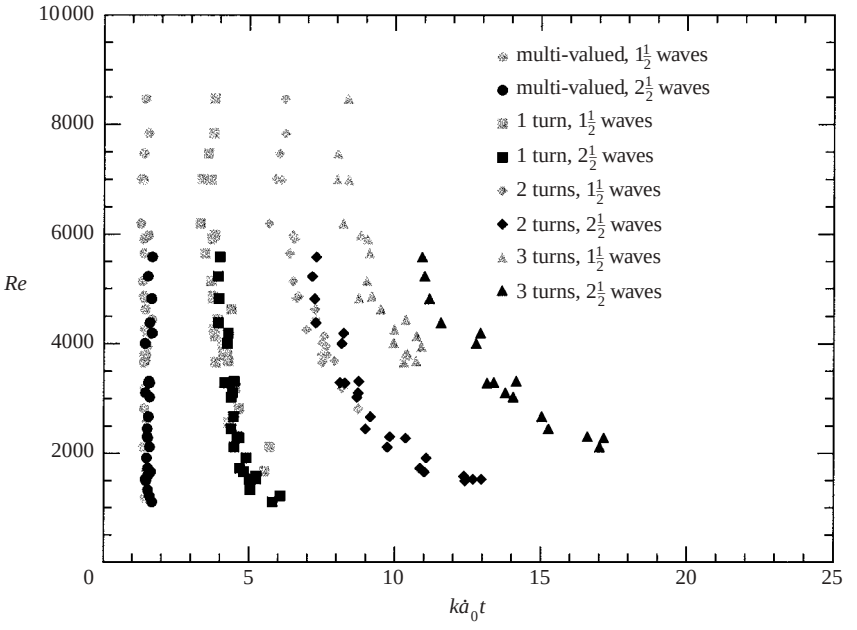

FIGURE 22. A plot of Reynolds number versus time describing the vortex core evolution.

from the initial folded condition. In figure 3(*b*), the interface is nearly vertical, and the vortex core has completed slightly more than 1 turn in figure 3(*e*), and slightly more than 2 turns in figure 3(*h*). The vortex core shown in figure 4 has completed slightly over 2 turns. Note that this definition yields a nearly constant time between turns and thus a constant rotation rate.

Figure 22 shows that the interface becomes multi-valued at $k\dot{a}_0 t \cong 1.5$ for all the experiments in the Reynolds number range tested for both the $1\frac{1}{2}$ and $2\frac{1}{2}$ wave cases. The time to complete 1, 2 and 3 turns appears to be independent of the Reynolds number for experiments with Reynolds numbers greater than 6000 over the times investigated. Therefore, the flow appears to be inertia dominated above a Reynolds number of 6000. At lower Reynolds numbers, the turning rate is observed to decrease as the Reynolds number is decreased indicating that the fluid viscosity is important. Thus, the primary effect of viscosity in these experiments is to reduce the number of coils observed in the vortex cores. Viscosity causes the vorticity to diffuse out from the vortex centres, leading to a decrease in the turning rate of the vortex cores. This process will eventually cause the vorticity from adjacent vortices to merge reducing the circulation, and thus, the overall growth rate. The fact that the amplitude measurements in this study appear to be independent of the Reynolds number suggests that vortex core sizes must still be small when compared to the vortex spacing for these experiments.

Note that the rotation rate measurements are very consistent for experiments carried out with a particular perturbation wavelength. However, there appears to be an inconsistency between experiments carried out with different wavelengths. This inconsistency is most easily observed in figure 22 when comparing the time to attain 3 turns for the $1\frac{1}{2}$ and $2\frac{1}{2}$ wave experiments. This discrepancy may have been caused by the fact that the dimensionless initial amplitudes of the shorter-wavelength experiments were generally larger than their longer-wavelength counterparts in order

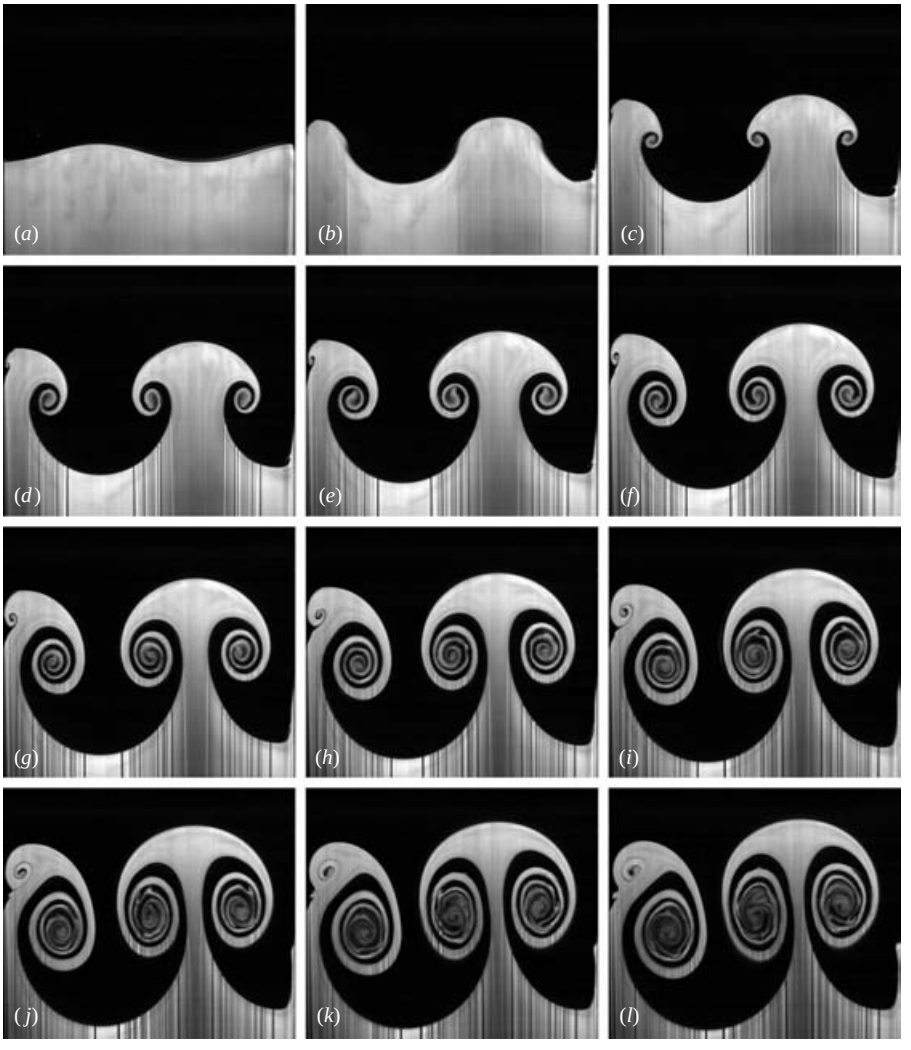

FIGURE 23. A sequence of images from a $1\frac{1}{2}$ wave experiment where the vortex core exhibits a secondary instability. Times relative to the midpoint of spring impact are (*a*) −24 ms, (*b*) 93 ms, (*c*) 176 ms, (*d*) 260 ms, (*e*) 343 ms, (*f*) 426 ms, (*g*) 510 ms, (*h*) 593 ms, (*i*) 677 ms, (*j*) 760 ms, (*k*) 843 ms, (*l*) 910 ms.

to obtain the same value of Reynolds number. In other words, a $2\frac{1}{2}$ wave experiment must have a larger dimensionless initial amplitude in order to achieve the same Reynolds number as a $1\frac{1}{2}$ wave experiment with the same impulsive acceleration. Thus, the effects of nonlinearity may have produced the small differences in the tuning rate observed in figure 22.

3.5.3. *Vortex instability*

Experiments carried out early in this investigation with relatively low values of the Reynolds number consistently showed a laminar spiralling of the interface around the vortex centre. However, later experiments carried out with significantly larger initial amplitudes and thus larger Reynolds numbers showed the appearance of an apparent secondary instability inside the vortex cores. Figure 23 shows a series of

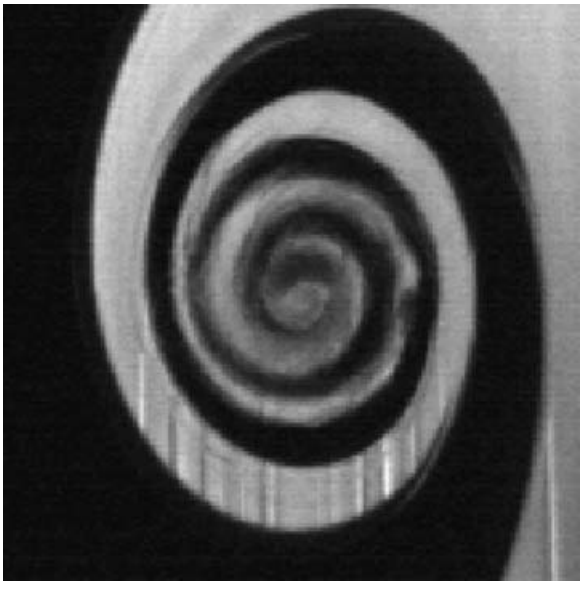

FIGURE 24. Close-up of a vortex core during the early stages of the secondary instability.

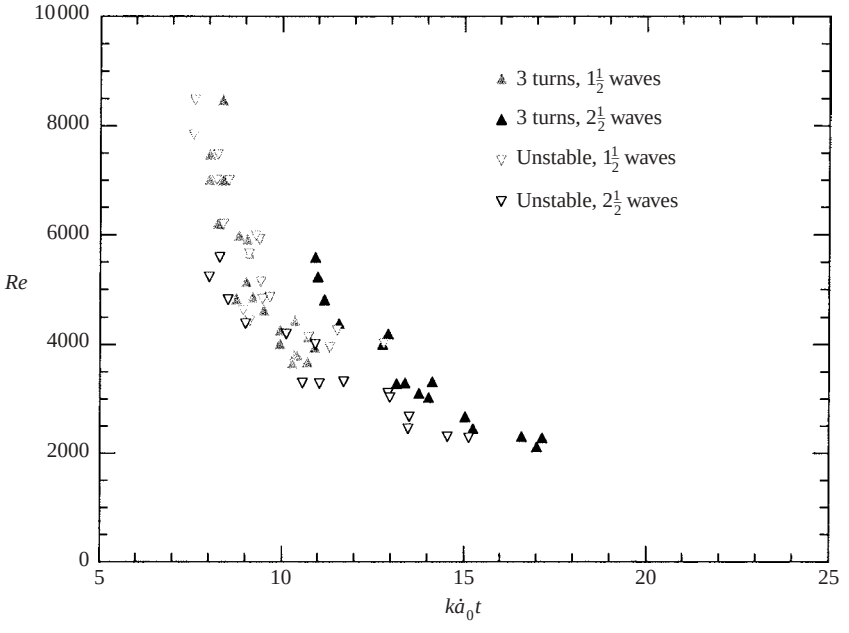

FIGURE 25. A plot of Reynolds number versus the time when the vortex core becomes unstable. Also shown are times when the vortex completes 3 turns.

images with $ka_i = 0.29$ and a Reynolds number of 4830 exhibiting this behaviour. The instability initially develops very similarly to the lower-amplitude cases. However, at figure 23(*h*), we can see the beginning of a secondary instability in the core of the vortex. By figure 23(*k*), the instability has spread throughout the core and the interface is no longer sharp, indicating that the fluids have begun to mix on a smaller

scale. Thus, it appears that this is the beginning of the transition to turbulence of the vortex cores.

Figure 24 shows a close-up of the core of an unstable vortex. The secondary instability initially takes the form of waves superimposed on the core spiral. These waves initiate near the centre of the core and grow in size and extent until all layers of the core spiral are affected. The non-dimensional time when the amplitude of these secondary instability waves is equal to the spiral thickness is shown in figure 25 versus the Reynolds number. Also shown is the dimensionless duration of the experiments in which the vortices remained stable throughout the experiment. We can clearly see that the experiments with larger Reynolds numbers develop the secondary instability sooner. Furthermore, this transition time appears to be correlated well to the time when the core has made approximately three complete turns.

4. Conclusions

Incompressible Richtmyer–Meshkov instability is studied in a novel experimental apparatus that allows for a quantitative analysis of the two-dimensional instability from the early linear stages, through the nonlinear regime, and into the initial stages of the transition to turbulence. Miscible liquids with moderate Atwood number were employed in this investigation. The use of liquids avoided many of the experimental difficulties previously limiting the study of the RM instability. The instability was generated by elastically bouncing a fluid-filled container off a vertical spring, imparting an impulsive acceleration. The subsequent free-fall permitted the instability to evolve in the absence of gravity far into the nonlinear stages. Planar laser-induced fluorescence allowed for extremely clear observations of the flow through the nonlinear regime.

Amplitude measurements are found to be in excellent agreement with linear stability theory for small amplitudes, differing by less than 10% up to a non-dimensional time $k\dot{a}_0 t$ of 0.7. Linear stability theory also shows excellent agreement for multi-mode experiments until the interface became multi-valued. The fourth-order single-mode perturbation solution of Zhang & Sohn (1997) is found to provide good agreement with amplitude measurements up to $k\dot{a}_0 t$ of 1.3. Zhang & Sohn's Padé approximation to their perturbation solution is found to extend the range of agreement for amplitude up to $k\dot{a}_0 t$ of 3. A discrete vortex model (Jacobs & Sheeley 1996) and the model of Sadot *et al.* (1998) are also compared to experimental amplitudes in the nonlinear regime. These two models are shown to be within 10% of the amplitude measurements up to $k\dot{a}_0 t$ of 30. The best agreement between experiments and theory is obtained from Sadot *et al.*'s model modified by using a new estimate for the asymptotic velocity.

Previous studies have not considered the influence of Reynolds number on the RM instability. This study examines the effects of Reynolds number defined using the vortex circulation. The time dependence of the overall perturbation amplitude is found to be independent of Reynolds number. However, the evolution of the vortex cores is found to be influenced by the Reynolds number when its value is sufficiently low. For the time duration studied, experiments with Reynolds numbers greater than 6000 are found to be independent of Reynolds number, indicating the flow is inertia dominated. Decreasing Reynolds number is found to lower the vortex turning rate. A secondary instability is observed to occur in the vortex cores of experiments with higher values of the Reynolds number. The time when the secondary instability was

first manifest appears to correlate well with the Reynolds number and is observed to occur when the core has made approximately three complete turns.

The experiments presented here demonstrate the merit of low-speed incompressible experiments for the study of RM instability. Low-speed incompressible experiments are in many respects notably superior to the more popular shock-tube experiments. For example, liquid experiments allow the generation of a sharp well-defined membraneless interface between the two fluids, an accomplishment currently unachievable in shock-tube experiments. Furthermore, the highly resolved motion sequences in these experiments could only be acquired using a video camera that travels with the unstable interface, a process that would be impossible to implement in shock-tube experiments.

The well-defined initial conditions combined with the imaging advantages have allowed these experiments to yield the most highly resolved motion sequences of the RM instability to date. In addition, the dimensionless times achieved in this experiment are three times greater that the longest duration shock-tube experiments. Thus, these experiments provide benchmark data for the comparison of numerical codes and nonlinear models of the late-time development of RM instability. The quality of the experimental image sequences has also allowed for the quantification of the effects of the Reynolds number on the instability including the development of a criterion for the occurrence of a secondary instability in the vortex cores. Although these experiments are incompressible, the results are applicable to many compressible situations that behave in an incompressible fashion after the shock waves have passed. These experiments also have moderate values of the Reynolds number. However, this study has shown that the effects of Reynolds number are confined to the vortex cores and have insignificant influence in the instability growth rate. Thus, the amplitude measurements presented here should be in agreement with experiments carried out at much larger Reynolds numbers and thus are useful to ICF and other higher-Reynolds-number applications.

This work was supported by Lawrence Livermore National Laboratory and by NASA's Microgravity Fluid Physics Program.

REFERENCES

Aleshin, A. N., Gamalii, E. G., Zaitsev, S. G., Lazareva, E. V., Lebo, I. G. & Rozanov, V. B. 1988 Nonlinear and transitional states in the onset of the Richtmyer–Meshkov instability. *Sov. Phys. Tech. Lett.* **14**, 466–468 [Russian: *Pis'ma Zh. Tekh. Fiz.* **14**, 1063–1067].

Alon, U., Hecht, J., Ofer, D. & Shvarts, D. 1995 Power laws and similarity of Rayleigh–Taylor and Richtmyer–Meshkov mixing fronts at all density ratios. *Phys. Rev. Lett.* **74**, 534–537.

Arnett, W. D., Bahcall, J. N., Kirshner, R. P. & Woosley, S. E. 1989 Supernova 1987A. *Annu. Rev. Astron. Astrophys.* **27**, 629–700.

Benjamin, R. F. 1992 Experimental observations of shock stability and shock-induced turbulence. In *Advances in Compressible Turbulent Mixing, Proceedings of the First International Workshop on the Physics of Compressible Turbulent Mixing* (ed. W. P. Dannevik, A. C. Buckingham & C. E. Leith), pp. 341–348. Lawrence Livermore National Laboratory, Conf-8810234.

Benjamin, R. F. & Fritz, J. N. 1987 Shock loading a rippled interface between liquids of differenct densities. *Phys. Fluids* **30**, 331–336.

Bonazza, R. & Sturtevant, B. 1996 X-ray measurements of growth rates at a gas interface accelerated by shock waves. *Phys. Fluids* **8**, 2496–2512.

Brouillette, M. & Sturtevant, B. 1994 Experiments on the Richtymyer–Meshkov instability: single-scale perturbations on a continuous interface. *J. Fluid Mech.* **263**, 271–292.

Budzinski, J. M., Benjamin, R. F. & Jacobs, J. W. 1994 Influence of initial conditions on the flow patterns of a shock-accelerated thin fluid layer. *Phys. Fluids* **6**, 3510–3512.

Burrows, A., Hayes, J. & Fryxell, B. A. 1995 On the nature of core-collapse supernova explosions. *Astrophys. J.* **450**, 830–850.

Cavailler, C., Mercier, P., Rodriguez, G. & Haas, J. F. 1990 A new vertical shock tube for Rayleigh–Taylor instability measurements. *Proc. 17th ISSWST at Bethlehem PA*, *Current Topics in Shock Waves* (ed. Y. Kim), p. 564.

Curran, E., Heiser, W. & Pratt, D. 1996 Fluid phenomena in scramjet combustion systems. *Annu. Rev. Fluid Mech.* **28**, 323–360.

Dimonte, G., Frerking, C. E. & Schneider, M. 1995 Richtmyer–Meshkov instability in the turbulent regime. *Phys. Rev. Lett.* **74**, 4855–4858.

Dimonte, G. & Remington, B. 1993 Richtmyer–Meshkov experiments on the Nova laser at high compression. *Phys. Rev. Lett.* **70**, 1806–1809.

Dimonte, G. & Schneider, M. 1997 Turbulent Richtmyer–Meshkov instability experiments with strong radiatively driven shocks. *Phys. Plasmas* **4**, 4347–4357.

Dimonte, G. & Schneider, M. 2000 Density ratio dependence of Rayleigh–Taylor mixing for sustained and impulsive acceleration histories. *Phys. Fluids* **12**, 304–321.

Farley, D. R., Peyser, T. A., Logory, L. M., Murray, S. D. & Burke, E. W. 1999 High Mach number mix instability experiments of an unstable density interface using a single-mode, nonlinear initial perturbation. *Phys. Plasmas* **6**, 4304–4317.

Haan, S. W. 1991 Weakly nonlinear hydrodynamic instabilities in inertial fusion. *Phys. Fluids* B **3**, 2349–2355.

Hecht, J., Alon, U. & Shvarts, D. 1994 Potential flow models of Rayleigh–Taylor and Richtmyer–Meshkov bubble fronts. *Phys. Fluids* **6**, 4019–4030.

Hogan, W. J., Bangerter, R. & Kulcinski, G. L. 1992 Energy from inertial fusion. *Phys. Today* **45**, 42–50.

Holmes, R. L., Dimonte, G., Fryxell, B., Gittings, M. L., Grove, J. W., Schnieder, M., Sharp, D. H., Velikovich, A. L., Weaver, R. P. & Zhang, Q. 1999 Richtmyer–Meshkov instabiity growth: experiment, simulation, and theory. *J. Fluid Mech.* **389**, 55–79.

Jacobs, J. W., Jenkins, D. G., Klein, D. L. & Benjamin, R. F. 1995 Nonlinear growth of the shock-accelerated instability of a thin fluid layer. *J. Fluid Mech.* **295**, 23–42.

Jacobs, J. W., Klein, D. L., Jenkins, D. G. & Benjamin, R. F. 1993 Instability growth patterns of a shock-accelerated thin fluid layer. *Phys. Rev. Lett.* **70**, 583–586.

Jacobs, J. W. & Sheeley, J. M. 1996 Experimental study of incompressible Richtmyer–Meshkov instability. *Phys. Fluids* **8**, 405–415.

Jones, M. A. & Jacobs, J. W. 1997 A membraneless experiment for the study of Richtmyer–Meshkov instability of a shock-accelerated gas interface. *Phys. Fluids* **9**, 3078–3085.

Lindl, J. D. 1995 Development of the indirect-drive approach to inertial confinement fusion and the target physics basis for ignition and gain. *Phys. Plasmas* **2**, 3933–4024.

Lindl, J. D., McCrory, R. L. & Campbell, E. M. 1992 Progress toward ignition and burn propagation in inertial confinement fusion. *Phys. Today* **45**, 32–40.

McCall, G. H. 1983 Laser-driven implosion experiments. *Plasma Phys.* **25**, 237–285.

Markstein, G. H. 1957 A shock tube study of flame front–pressure wave interaction. In *6th Intl Symp on Combustion*, Reinhold. pp. 387–398.

Meshkov, E. E. 1969 Instability of the interface of two gases accelerated by a shock wave. *Izv. Akad. Nauk SSSR Mekh. Zhid. i Gaza* **4**, 151–157.

Oron, D., Arazi, L., Kartoon, D., Rikanati, A., Alon, U. & Shvarts, D. 2001 Dimensionality dependence of the Rayleigh–Taylor and Richtmyer–Meshkov instability late-time scaling laws. *Phys. Plasmas* **8**, 2883–2889.

Peyser, T. A., Miller, P. L., Stry, P. E., Budil, K. S., Burke, E. W., Wojtowicz, D. A., Griswold, D. L., Hammel, B. A. & Phillion, D. W. 1995 Measurement of radiation-driven shock-induced mixing from nonlinear initial perturbations. *Phys. Rev. Lett.* **75**, 2332–2335.

Rayleigh, Lord 1900 *The Scientific Papers of Lord Rayleigh*, vol. 2. Cambridge University Press.

Remington, B. A., Weber, S. V., Marinak, M. M., Haan, S. W., Kilkenny, J. D., Wallace, R. & Dimonte, G. 1994 Multimode Rayleigh–Taylor experiments on Nova. *Phys. Rev. Lett.* **73**, 545–548.

Richtmyer, R. D. 1960 Taylor instability in shock acceleration of compressible fluids. *Commun. Pure Appl. Maths* **13**, 297–319.

Rightley, P. M., Vorobieff, P., Martin, R. & Benjamin, R. F. 1999 Experimental observations of the mixing transition in a shock-accelerated gas curtain. *Phys. Fluids* **11**, 186–200.

Sadot, O., Erez, L., Alon, U., Levin, L. A., Erex, G., Ben-Dor, G. & Shvarts, D. 1998 Study of nonlinear evolution of single-mode and two-bubble interaction under Richtmyer–Meshkov instability. *Phys. Rev. Lett.* **80**, 1654–1657.

Takabe, H. & Yamamoto, A. 1991 Reduction of turbulent mixing at the ablation front of fusion targets. *Phys. Rev.* A **44**, 5142–5149.

Taylor, G. I. 1950 The instability of liquid surfaces when accelerated in a direction perpendicular to their planes. *Proc. R. Soc. Lond.* A **201**, 192–196.

Vassilenko, A. M., Buryakov, O. V., Kuropatenko, V. F., Olkhovskaya, V. I., Ratnikov, V. P. & Jakovlev, V. G. 1992 Experimental research of gravitational instability and turbulization of flow at the noble gases interface. In *Advances in Compressible Turbulent Mixing, First International Workshop on the Physics of Compressible Turbulent Mixing* (ed. W. P. Dannevik, A. C. Buckingham & C. E. Leith), pp. 581–606. Lawrence Livermore National Laboratory, Conf-8810234.

Waddell, J. T., Niederhaus, C. E. & Jacobs, J. W. 2001 Experimental study of Rayleigh–Taylor instability: low Atwood number liquid systems with single-mode initial perturbations. *Phys. Fluids* **13**, 1263–1273.

Zabusky, N. J. 1999 Vortex paradigm for accelerated inhomogeneous flows: visiometrics for the Rayleigh–Taylor and Richtmyer–Meshkov environments. *Annu. Rev. Fluid Mech.* **31**, 495–536.

Zhang, Q. & Sohn, S. 1997 Nonlinear theory of unstable fluid mixing driven by shock wave. *Phys. Fluids* **9**, 1106–1124.